Vps35 loss promotes hyperresorptive osteoclastogenesis and osteoporosis via sustained RANKL signaling

Wen-Fang Xia,[1,2,3,5] Fu-Lei Tang,[1,2,3] Lei Xiong,[1,2,3] Shan Xiong,[1,2,3] Ji-Ung Jung,[1,2] Dae-Hoon Lee,[1,2] Xing-Sheng Li,[4] Xu Feng,[4] Lin Mei,[1,2] and Wen-Cheng Xiong[1,2,3]

[1]Institute of Molecular Medicine and Genetics and [2]Department of Neurology, Medical College of Georgia, Georgia Health Sciences University, Augusta, GA 30912
[3]Charlie Norwood Veterans Administration Medical Center, Augusta, GA 30912
[4]Department of Pathology, The University of Alabama at Birmingham, Birmingham, AL 35294
[5]Department of Endocrinology, Union Hospital, Tongji Medical College, Huazhong University of Science and Technology, Wuhan 430022, China

Receptor activator of NF-κB (RANK) plays a critical role in osteoclastogenesis, an essential process for the initiation of bone remodeling to maintain healthy bone mass and structure. Although the signaling and function of RANK have been investigated extensively, much less is known about the negative regulatory mechanisms of its signaling. We demonstrate in this paper that RANK trafficking, signaling, and function are regulated by VPS35, a major component of the retromer essential for selective endosome to Golgi retrieval of membrane proteins. VPS35 loss of function altered RANK ligand (RANKL)–induced RANK distribution, enhanced RANKL sensitivity, sustained RANKL signaling, and increased hyperresorptive osteoclast (OC) formation. Hemizygous deletion of the Vps35 gene in mice promoted hyperresorptive osteoclastogenesis, decreased bone formation, and caused a subsequent osteoporotic deficit, including decreased trabecular bone volumes and reduced trabecular thickness and density in long bones. These results indicate that VPS35 critically deregulates RANK signaling, thus restraining increased formation of hyperresorptive OCs and preventing osteoporotic deficits.

Introduction

Osteoclast (OC) formation and activation are critical events for the maintenance of normal bone mass and structure. OCs are formed from hematopoietic lineage cells and activated to resorb bone by numerous factors derived from osteoblast (OB) lineage cells (Tanaka et al., 1993; Lacey et al., 1998; Yasuda et al., 1998; Boyle et al., 2003; Teitelbaum and Ross, 2003; Crockett et al., 2011; Maeda et al., 2012). Among the factors identified to promote osteoclastogenesis, receptor activator of NF-κB (RANK) ligand (RANKL) is best studied. RANKL, produced by OB lineage cells (e.g., osteocytes; Nakashima et al., 2011; Xiong et al., 2011b), stimulates RANK, a TNF receptor family member in OC lineage cells, and thus activates NF-κB, Erk1/2, and Akt pathways, which leads to subsequent expression of genes necessary for OC differentiation, activation, and survival (Yasuda et al., 1998; Teitelbaum, 2000; Novack, 2011). Although the signaling and function of RANK have been studied extensively, less is known about regulatory mechanisms of RANK receptor trafficking and stability.

VPS35 is a critical component of the retromer protein complex that is essential for retrieval of transmembrane proteins from endosome to Golgi apparatus (Seaman et al., 1997; Bonifacino and Hurley, 2008; McGough and Cullen, 2011). Retromer has two subcomplexes: one for cargo selection and another one for membrane deformation (Seaman, 2005). VPS35 belongs to the cargo-selective subcomplex, which contains a trimer of vacuolar protein-sorting proteins, VPS35, VPS29, and VPS26. Numerous transmembrane proteins/receptors have been identified to be retromer cargos, which include VPS10/sortilin

W.-F. Xia and F.-L. Tang contributed equally to this paper.

Correspondence to Wen-Cheng Xiong: wxiong@georgiahealth.edu

Abbreviations used in this paper: ALP, alkaline phosphatase; β-gal, β-galactosidase; BFR, bone formation rate; BMM, bone marrow macrophage; BMSC, bone marrow stromal cell; BV, bone volume; MAR, mineral apposition rate; M-CSF, macrophage colony-stimulating factor; μCT, microcomputer tomographic; OB, osteoblast; OC, osteoclast; PE, phycoerythrin; PYD, pyridinoline; RAGE, receptor for advanced glycation end products; RANK, receptor activator of NF-κB; RANKL, RANK ligand; ROI, region on interest; TRAP, tartrate-resistant acid phosphatase; TV, total volume; WT, wild type.

The Rockefeller University Press $30.00
J. Cell Biol. Vol. 200 No. 6 821–837
www.jcb.org/cgi/doi/10.1083/jcb.201207154

family proteins (Seaman, 2005), cation-independent M6P receptor (Seaman, 2004), mammalian iron transporter DMT1(Tabuchi et al., 2010), *Caenorhabditis elegans* phagocytosis receptor Ced1(Chen et al., 2010a), amyloid precursor protein (Vieira et al., 2010), BACE1 (amyloid precursor protein processing β1 secretase; Wen et al., 2011), Wntless (Belenkaya et al., 2008; Pan et al., 2008; Yang et al., 2008), β2-adrenergic receptor (Temkin et al., 2011), and PTH1R (type 1 receptor for parathyroid hormone; Feinstein et al., 2011). Interestingly, some of the retromer cargoes (e.g., PTH1R and Wntless) are important regulators of bone remodeling. However, the function of the retromer in this event has not been investigated.

Here, we provide evidence for a critical role of VPS35 in bone remodeling. VPS35 is highly expressed in macrophages and OCs as well as OBs. Microcomputer tomographic (μCT) analysis indicated that VPS35 loss of function in mice led to osteoporotic deficits. Concomitantly, bone formation was decreased, and bone resorption and OC formation were increased in VPS35 mutant mice. We further investigated the effect of Vps35 loss on RANKL signaling in macrophages and found that VPS35 is necessary to prevent sustained RANK activation. Cell biological experiments suggest that VPS35 may inactivate RANK signaling by promoting RANKL-induced RANK endosome to Golgi translocation. Collectively, these results suggest that VPS35 is required for deregulation of RANKL-driven signaling and suppression of OC formation, revealing a novel mechanism to negatively regulate RANK signaling and demonstrating a critical role for VPS35 in maintaining a balanced bone remodeling.

Results

Osteoporotic deficits in Vps35$^{+/m}$ mice

To investigate functions of VPS35/retromer in osteoclastogenesis, we first examined whether Vps35 is expressed in bone marrow cells by taking advantage of the Vps35$^{+/m}$ mice. In these mice, the LacZ gene was knocked in in the intron of the Vps35 gene (Wen et al., 2011); thus, LacZ expression is controlled by Vps35's promoter. The LacZ activity was detected along the endosteal surface of the trabecular and cortical bones in the femurs of neonatal Vps35$^{+/m}$ mice but undetectable in Vps35$^{+/+}$ mice and the growth plates of Vps35$^{+/m}$ mice (Fig. 1, A and B; and Fig. S1 A). Some of these β-galactosidase (β-gal)–positive cells were tartrate-resistant acid phosphatase (TRAP) positive (Fig. S1 B) and appeared to be in association with the basic multicellular units, which consist of the closely contacted OB and OC lineage cells (Parfitt et al., 1987). To test whether Vps35 is expressed in OB and OC lineage cells, bone marrow stromal cells (BMSCs; precursors of OBs) and bone marrow macrophages (BMMs; precursors of OCs) were harvested from Vps35$^{+/+}$ and Vps35$^{+/m}$ mice and examined for their LacZ activity as well as VPS35 protein expression by Western blot analysis (Fig. 1, C–F). VPS35's expression and its subcellular distribution in OCs differentiated from wild-type (WT) and mutant BMMs were also examined by immunostaining analysis (Fig. 1 G). The results from these experiments demonstrated that VPS35 is highly expressed in BMMs and OCs, in addition to OB lineage cells (Fig. 1, C–F), and a fraction of VPS35 (∼34%) appeared to be colocalized with LAMP1-positive late endosomes or early lysosomes in OCs (Fig. 1 G).

We next asked whether Vps35 is required for maintaining bone mass by μCT analysis of femur bone mass and structure of adult (3 mo old) Vps35$^{+/+}$ and Vps35$^{+/m}$ mice. Remarkably, a decreased volume of trabecular bones with an enlarged bone marrow cavity was observed in Vps35$^{+/m}$ mice as compared with that of Vps35$^{+/+}$ littermates (Fig. 2, A and B). In addition, trabecular numbers, trabecular thickness, trabecular separation, and trabecular connectivity density were all deficient in Vps35$^{+/m}$ versus WT control mice (Fig. 2 B). Cortical bone volumes (BVs) were relatively normal in the mutant femurs (Fig. 2 B). Further observations by hematoxylin and eosin staining analysis provided additional support for the decrease of trabecular BVs in both femur and tibia bones of 3-mo-old Vps35$^{+/m}$ mice (Fig. 2, C–E). In contrast, safranin O staining analysis revealed a normal or unchanged morphology at the growth plates of Vps35$^{+/m}$ mice (Fig. 2 D), suggesting little or no effect of VPS35/retromer on chondrocyte differentiation and function. These phenotypes are reminiscent of the osteoporotic skeleton pathology, suggesting a critical role for VPS35/retromer in regulating bone remodeling.

Decrease of bone formation in Vps35$^{+/m}$ mice

The osteoporotic deficits may result from decreased bone formation and/or increased OC genesis and activation. We thus examined both events in Vps35$^{+/m}$ and Vps35$^{+/+}$ mice. The bone formation was first evaluated by two injections of the fluorochrome labels, calcein green and alizarin red, separated by a 12-d interval, to littermates of neonatal WT and Vps35$^{+/m}$ mice. The mineral apposition rate (MAR) and bone formation rate (BFR) of both groups were assessed in nondecalcified histological sections of femurs and tibia of the injected mice. The endocortical, but not periosteal, MAR as well as endocortical BFR was slightly reduced in the mutant mice (Fig. 3, A and B), suggesting a decreased endocortical bone formation. In addition, the endocortical, but not periosteal, bone surface labeled by the fluorochrome was also reduced in the mutant mice (Fig. 3 B). The decrease in bone formation was further supported by the reduced levels of serum osteocalcin, a bone formation marker, in Vps35$^{+/m}$ mice (Fig. 3 C). We next performed an in vitro osteoblastogenesis assay of BMSCs derived from 2-mo-old Vps35$^{+/m}$ and Vps35$^{+/+}$ mice. No significant difference of in vitro OB differentiation, assessed by alkaline phosphatase (ALP) staining of the WT and Vps35$^{+/m}$ OB cultures, was detected (Fig. 3, D and E). Thus, the reduced bone formation in Vps35$^{+/m}$ mice may be caused by complex mechanisms.

Increase of OC formation and activity in Vps35$^{+/m}$ mice and Vps35$^{+/m}$ BMM culture

To further understand how Vps35 regulates bone mass, we examined bone resorption in Vps35$^{+/m}$ and Vps35$^{+/+}$ mice. This process was first evaluated by measurement of serum levels of deoxypyridinoline (PYD), a bone resorption marker. Serum PYD levels were markedly increased in Vps35$^{+/m}$ mice (Fig. 4 A).

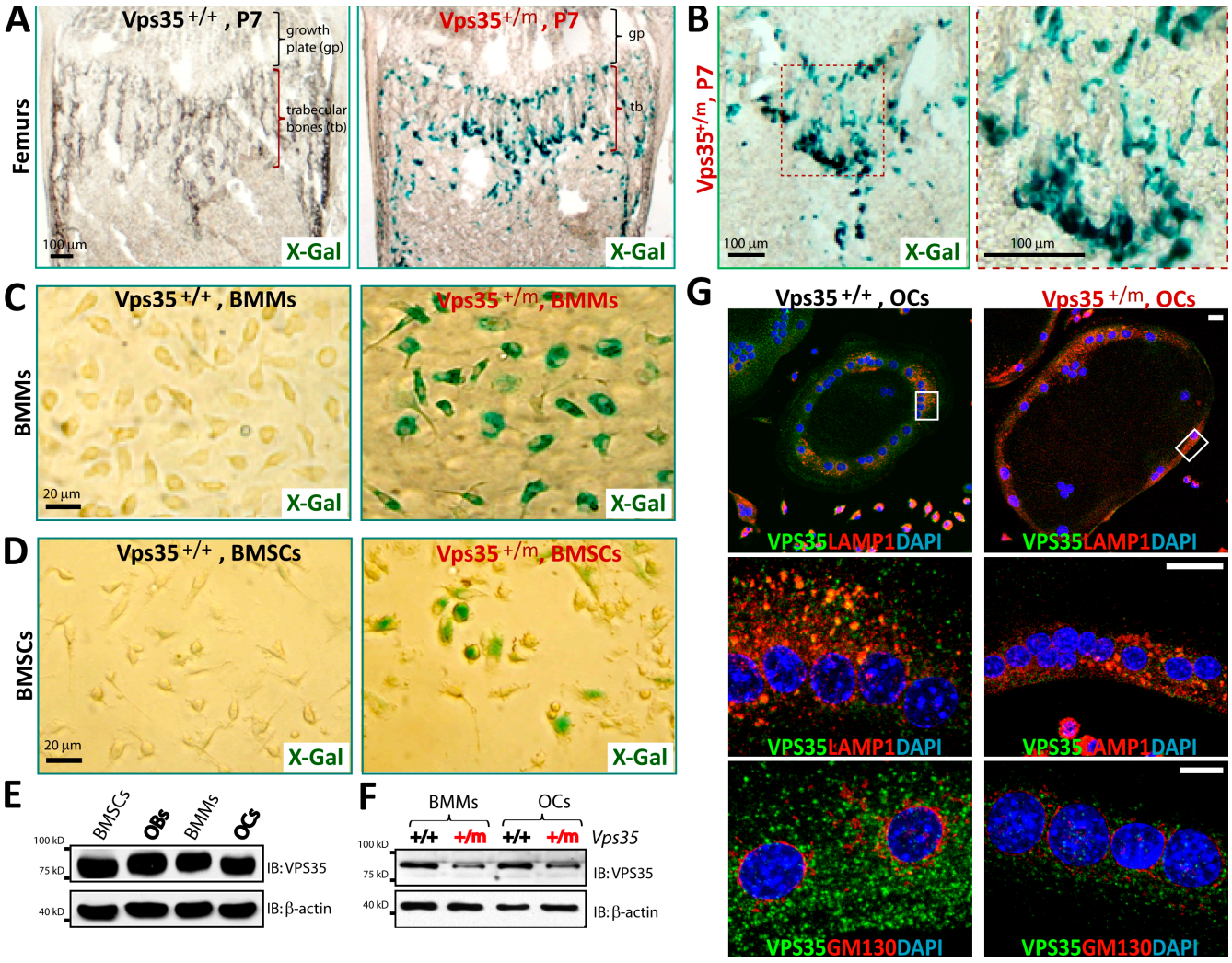

Figure 1. **Expression of VPS35 in OC and OB lineage cells.** (A–D) Detection of enzymatic LacZ activity in femurs of P7 Vps35$^{+/m}$, but not Vps35$^{+/+}$, mice (A and B) and in purified bone marrow macrophages (BMMs; C) and mesenchymal stromal cells (BMSCs; D) from 1-mo-old Vps35$^{+/m}$, but not Vps35$^{+/+}$, mice. In B, the image marked with a red dot square was amplified and shown in the right. In C and D, ∼50% of cells (BMSCs and BMMs) were positive for LacZ, as they were from Vps35$^{+/m}$ mice. (E and F) Western blot analysis of VPS35 protein levels in lysates of BMSCs, osteoblasts (OBs), BMMs, and osteoclasts (OCs) as indicated. In F, OBs or OCs from Vps35$^{+/m}$ mice showed ∼50% reduction of VPS35, reconfirming the loss of Vps35 in the mutant mice and the antibody specificity. IB, immunoblot. (G) Coimmunostaining analysis of VPS35 with LAMP1 (a marker for late endosomes and early lysosomes) or GM130 (a marker for Golgi) in Vps35$^{+/+}$ and Vps35$^{+/m}$ OCs. Images marked with white rectangles were amplified and shown in the middle images. Partial colocalizations of VPS35 with LAMP1 (∼34%) and GM130 (∼3%) were detected. VPS35 staining appeared to be specific, as the signal was decreased in the Vps35$^{+/m}$ OCs. Bars, 20 μm.

Also increased was serum IL-6 (interleukin 6; Fig. 4 B), a cytokine frequently associated with the OC activation (Takeshita et al., 2002; Roodman and Windle, 2005). Interestingly, the increased serum levels of PYD and IL-6 were more obvious in 1-mo-old mutant mice (Fig. 4, A and B), in contrast from that of serum osteocalcin, which was more robust in 3-mo-old mutant mice (Fig. 3 A). These results thus suggest that the decreased bone formation in the mutant mice may follow the initial increase of bone resorption. We next asked whether the increased bone resorption is caused by an increased OC genesis in the mutant mice. Bone histomorphological examinations showed a significant increase in the number of TRAP^{+} OCs per unit of bone surface in femurs of Vps35$^{+/m}$ mice, particularly at the neonatal stage (Fig. 4, C–G), correlating well with the increased bone resorption. Thus, these in vivo results demonstrate elevated OC formation and activation in Vps35 mutant mice during neonatal skeletal development.

We then asked whether VPS35 regulates OC formation in a cell-autonomous manner by in vitro osteoclastogenesis assay. Cultures of BMMs derived from Vps35$^{+/+}$ and Vps35$^{+/m}$ mice (1–2 mo old) were exposed to macrophage colony-stimulating factor (M-CSF) and RANKL for 7 d to induce OCs. The WT cultures formed TRAP-positive cells, and the typical multinucleated characteristics of in vitro–differentiated OCs were displayed (Fig. 5 A). Notably, Vps35$^{+/m}$ cultures showed even more and larger TRAP-positive OCs (Fig. 5, A and B). The enlarged OCs in Vps35$^{+/m}$ culture were further confirmed by phalloidin staining of actin ring structures in OCs (Fig. 5, C and D). We next asked whether these Vps35-deficient large OCs are active by examining their resorptive activity in culture and

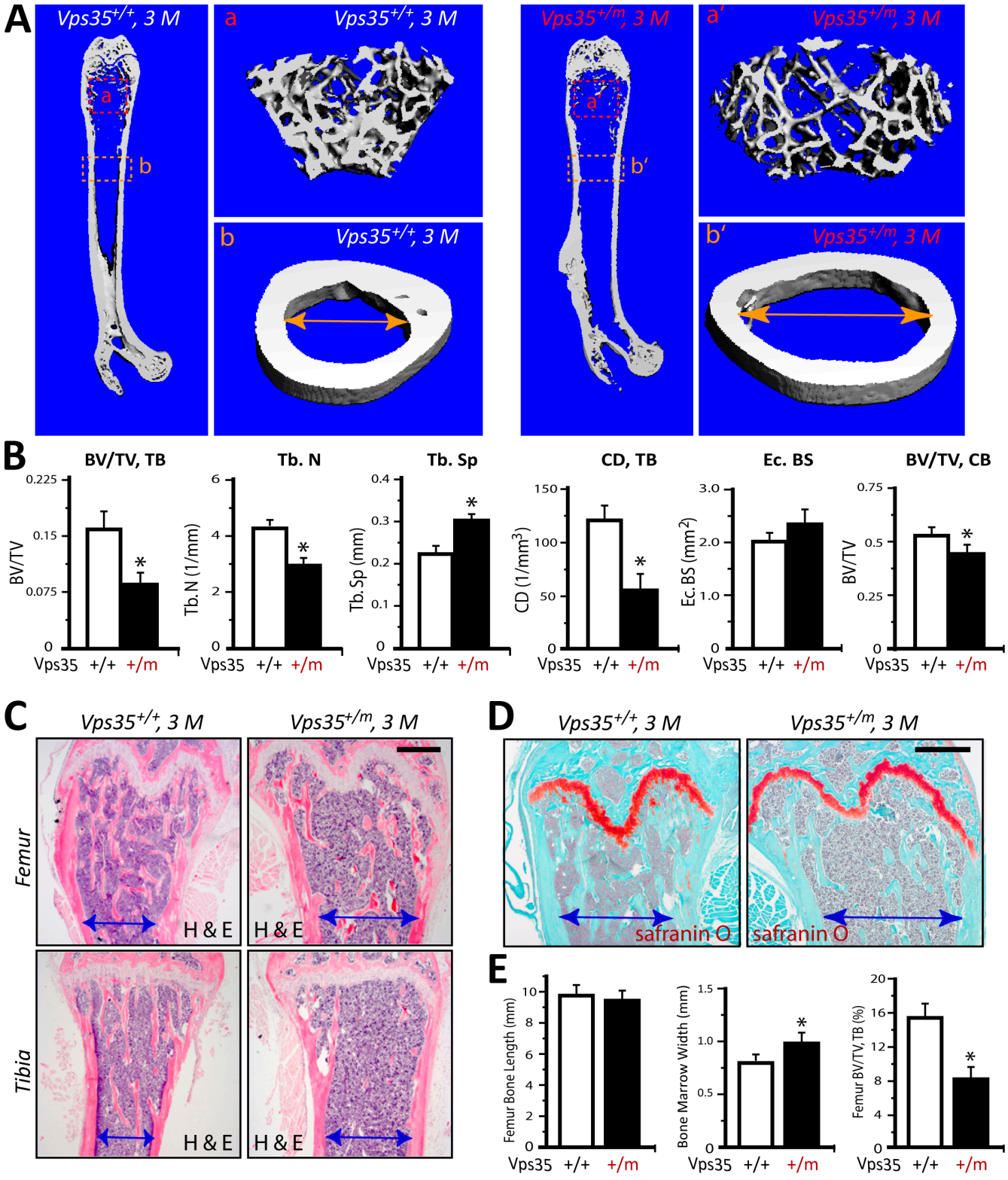

Figure 2. **Osteoporotic deficits in adult Vps35$^{+/m}$ mice.** (A and B) The µCT analysis of femurs from 3-mo-old Vps35$^{+/+}$ and Vps35$^{+/m}$ littermates. Five different male mice of each genotype were examined blindly. Representative images are shown in A. The 3D images shown on the right (a, a′, b, and b′) were derived from the marked corresponding regions of the femurs in the left images. Quantification analyses (n = 5) are presented in B. Note that the trabecular bone (tb) volumes over total volumes (BV/TV), the trabecular bone numbers (Tb.N), trabecular separation (Tb.Sp), and trabecular connectivity density (CD; normalized by TV [1/mm^3]) by direct model of µCT analysis were all deficient in Vps35$^{+/m}$ as compared with the WT control. The endocortical bone surface (Ec. BS) was slightly increased in the mutant, but no statistical significance was detected. The cortical BVs over TVs were decreased in the mutant mice. CB, cortical bone. (C–E) Histomorphological examinations by hematoxylin and eosin (H & E; C) and safranin O (D) staining analyses of femurs of 3-mo-old Vps35$^{+/+}$ and Vsp35$^{+/m}$ littermates. Representative images were shown in C and D. Bars, 500 µm. Bone marrow cavity diameters are marked. Quantification analyses of femur length and trabecular BV/TV are shown in E (n = 5 bone samples/each genotype). Means ± SD. *, P < 0.05, significant difference from the control littermates.

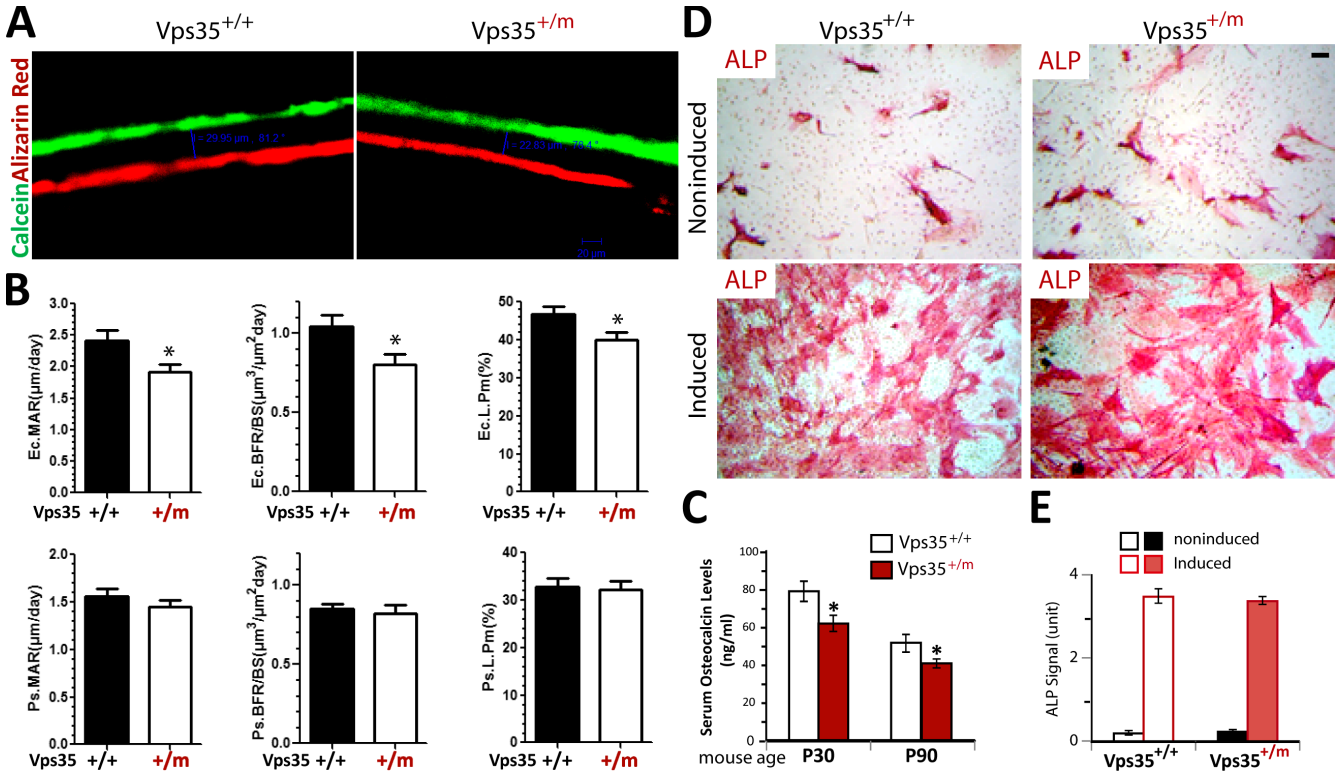

Figure 3. **Decreased bone formation in Vps35$^{+/m}$ mice, but not in Vps35$^{+/m}$, OB culture.** (A and B) Reduced bone formation in Vps35$^{+/m}$ mice detected by dynamic histomorphometric measurements of calcein and alizarin double-labeled femurs (see Materials and methods). Five male mice per genotype at age of P14 were injected with calcein followed by alizarin (12-d interval). 2 d after alizarin injection, mice were sacrificed (at P28). (A) Representative images of histological sections showing calcein and alizarin double labeling of endocortical bone in femur middiaphysis of Vps35$^{+/+}$ and Vps35$^{+/m}$ mice. (B) Endocortical mineral apposition rate (Ec. MAR), endocortical bone formation rate (Ec. BFR), and endocortical bone surface labeled show reductions in Vps35$^{+/m}$ femurs. However, periosteal (Ps.) MAR–, Ps. BFR–, and Ps. bone surface (BS)–labeled cells appeared to be normal. L.Pm, labeled perimeter. (C) Decreased bone formation in Vps35$^{+/m}$ mice observed by measurement of serum levels of osteocalcin in 1- and 3-mo-old Vps35$^{+/+}$ and Vps35$^{+/m}$ mice using ELISA assays (see Materials and methods). In B and C, the values of means ± SD from five different animals per genotype are shown. *, $P < 0.05$, significant difference from the control. (D and E) Normal in vitro OB differentiation of BMSCs derived from 2-mo-old Vps35$^{+/+}$ and Vps35$^{+/m}$ mice. (D) Representative images of ALP staining analysis of Vps35$^{+/+}$ and Vps35$^{+/m}$ OBs (day 14 OB culture of BMSCs isolated from 2-mo-old Vps35$^{+/+}$ and Vps35$^{+/m}$ femur bone marrows). Bars, 20 μm. (E) Quantitative analysis of the mean ALP activities (means ± SD from three different cultures) of Vps35$^{+/+}$ and Vps35$^{+/m}$ OBs.

by accessing their secretion of proteases, such as cathepsin D and cathepsin K, both critical enzymes for resorption. In line with the increased OC formation, a hyperresorptive activity with an increase in mean sizes of resorptive pits was detected in the mutant OC cultures (Fig. 5, E and F). In addition, increased levels of both cathepsin D and cathepsin K were detected in the medium, but not cell lysates, in Vps35$^{+/m}$ OCs as compared with that of Vps35$^{+/+}$ (Fig. 5, G and H). Thus, these in vitro results, in line with the in vivo observations, suggest a cell-autonomous function for VPS35 in suppressing hyperresorptive OC formation and activation.

Increased RANKL sensitivity and sustained RANKL-driven signaling in Vps35-deficient Raw264.7 cells and Vps35$^{+/m}$ BMMs

Given the importance of RANKL–RANK signaling in osteoclastogenesis, we examined whether RANKL sensitivity and signaling were altered in Vps35 mutant culture. BMMs from Vps35$^{+/+}$ and Vps35$^{+/m}$ mice were exposed to 10% of M-CSF with different concentrations of RANKL. Vps35$^{+/m}$ BMMs indeed showed a hypersensitivity to RANKL to differentiate into OCs (Fig. 6, A–C), which was more evident at low concentrations of RANKL treatment (e.g., 20 ng/ml; Fig. 6 A–D). No obvious difference was detected in terms of OC cell death between Vps35$^{+/+}$ and Vps35$^{+/m}$ culture (Fig. 6, A and E). These results further support a role for VPS35 in deregulating RANKL-induced osteoclastogenesis in a cell-autonomous manner.

To further understand how VPS35 negatively regulates RANKL-induced osteoclastogenesis, we examined RANKL-driven signaling events in macrophages infected with lentiviruses expressing control and shRNA-Vps35. The Raw264.7 cell line was first used because it survives without M-CSF and differentiates into OCs when exposed to RANKL only. In addition, Raw264.7 cells infected with lentiviruses of shRNA-Vps35 exhibited ~80–90% reduction of Vps35 expression (Fig. S2), whereas Vps35$^{+/m}$ BMM culture showed a <50% decrease of VPS35 levels (Fig. 1 G). RANKL-driven signaling events, including phosphorylation of Erk1/2, Akt, and IκB-α, were examined, as they are essential for the development of macrophages to mature OCs and for macrophage/OC survival (Lacey et al., 1998; Yasuda et al., 1998). As shown in Fig. 7, RANKL activation of NF-κB, assessed by IκB-α phosphorylation and degradation, and RANKL-driven phosphorylation of Erk1/2 and Akt were all sustained in Vps35-depleted

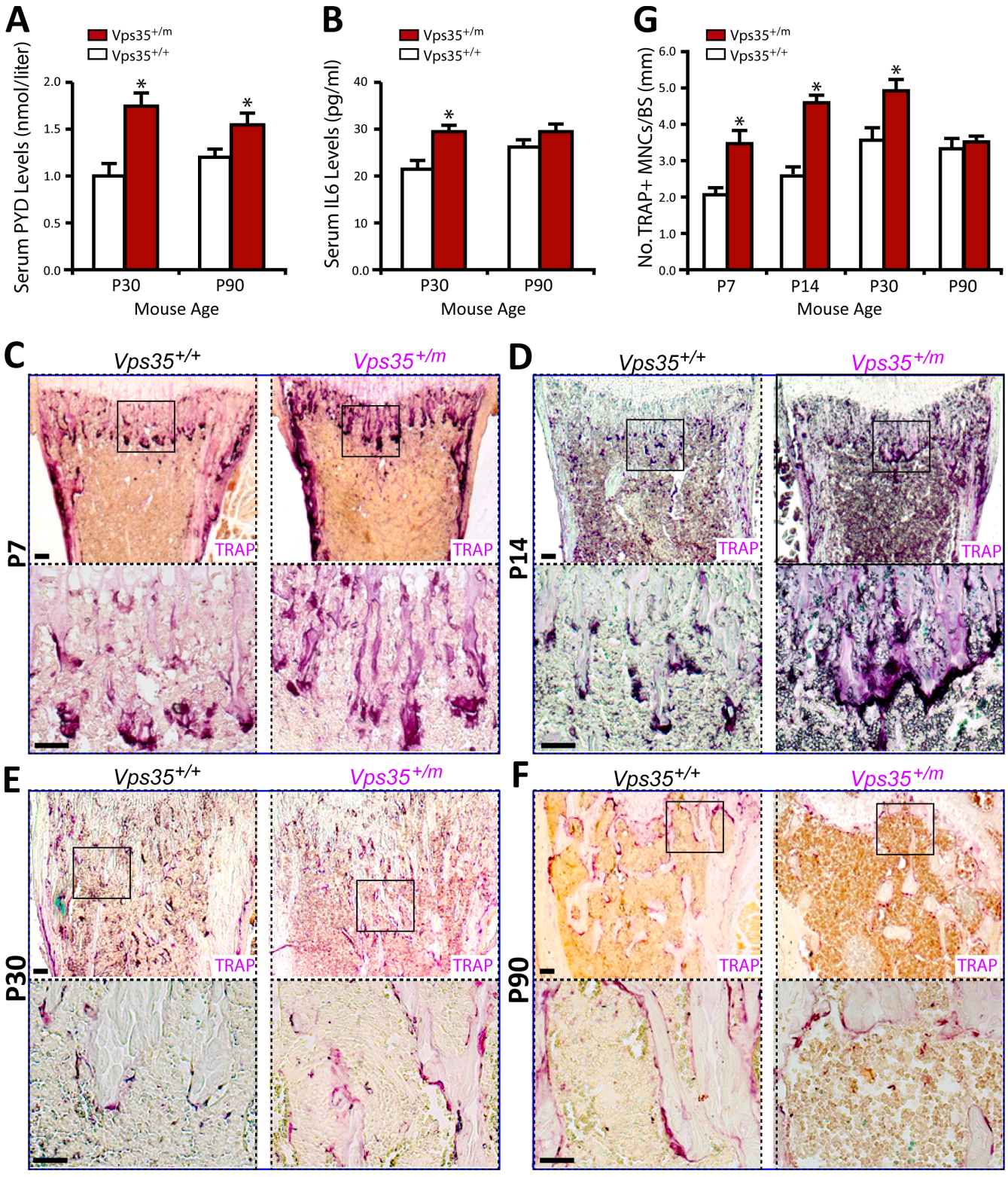

Figure 4. **Increased serum levels of PYD and IL-6 and OCs in Vps35$^{+/m}$ mice.** (A and B) Measurements of serum levels of PYD (A) and IL-6 (B) in 1- and 3-mo-old Vps35$^{+/+}$ and Vps35$^{+/m}$ mice by RIA and ELISA analyses, respectively. Six male mice per genotype per age group were measured. (C–G) TRAP staining analysis of femur sections from different aged Vps35$^{+/+}$ and Vps35$^{+/m}$ littermates (five mice per age group per genotype, both males and females). (C–F) Representative images of TRAP staining were shown. Images marked with black squares were amplified and shown in the bottom images. Bars, 100 µm. (G) The quantitative analysis of TRAP^{+} cells per unit bone surface (BS) was performed in trabecular bones of femurs from differently aged Vps35$^{+/+}$ and Vps35$^{+/m}$ mice. In A, B, and G, the values of means ± SD from five to six different animals are shown. *, $P < 0.05$, significant difference from WT control.

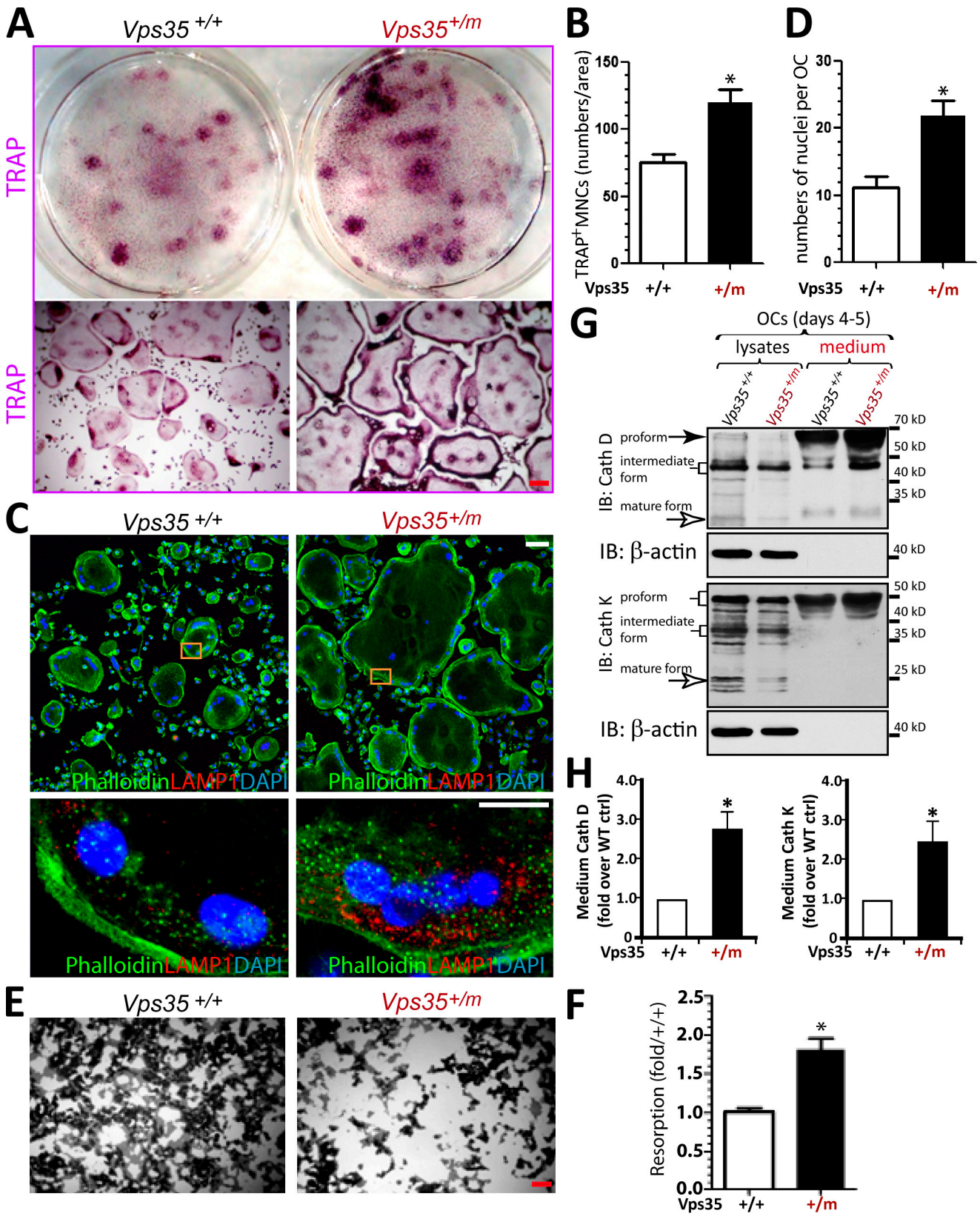

Figure 5. **Elevation of hyperresorptive osteoclastogenesis in Vps35$^{+/m}$ BMM culture.** (A–D) TRAP staining (A and B) and phalloidin staining (C and D) analyses of OCs. OCs were generated from BMMs derived from 1-mo-old Vps35$^{+/+}$ and Vps35$^{+/m}$ mice in the presence of 10% M-CSF and 100 ng/ml RANKL for 7 d. Representative images were shown in A and C. Quantitative analyses of the mean TRAP-positive multinuclei cell (MNC) density (count TRAP^{+} cells with more than three nuclei per cell per unit area), and nuclei numbers per OC cell were presented in B and D, respectively. (E and F) The in vitro resorptive activity of Vps35$^{+/+}$ and Vps35$^{+/m}$ OCs was revealed by Von Kossa staining of OCs cultured on coverslips coated with calcium phosphate matrix for 8 d. The resorbing activity was quantified based on mean resorbing area from E, normalized by Vps35$^{+/+}$ control, and shown in F. Bars, 30 µm.

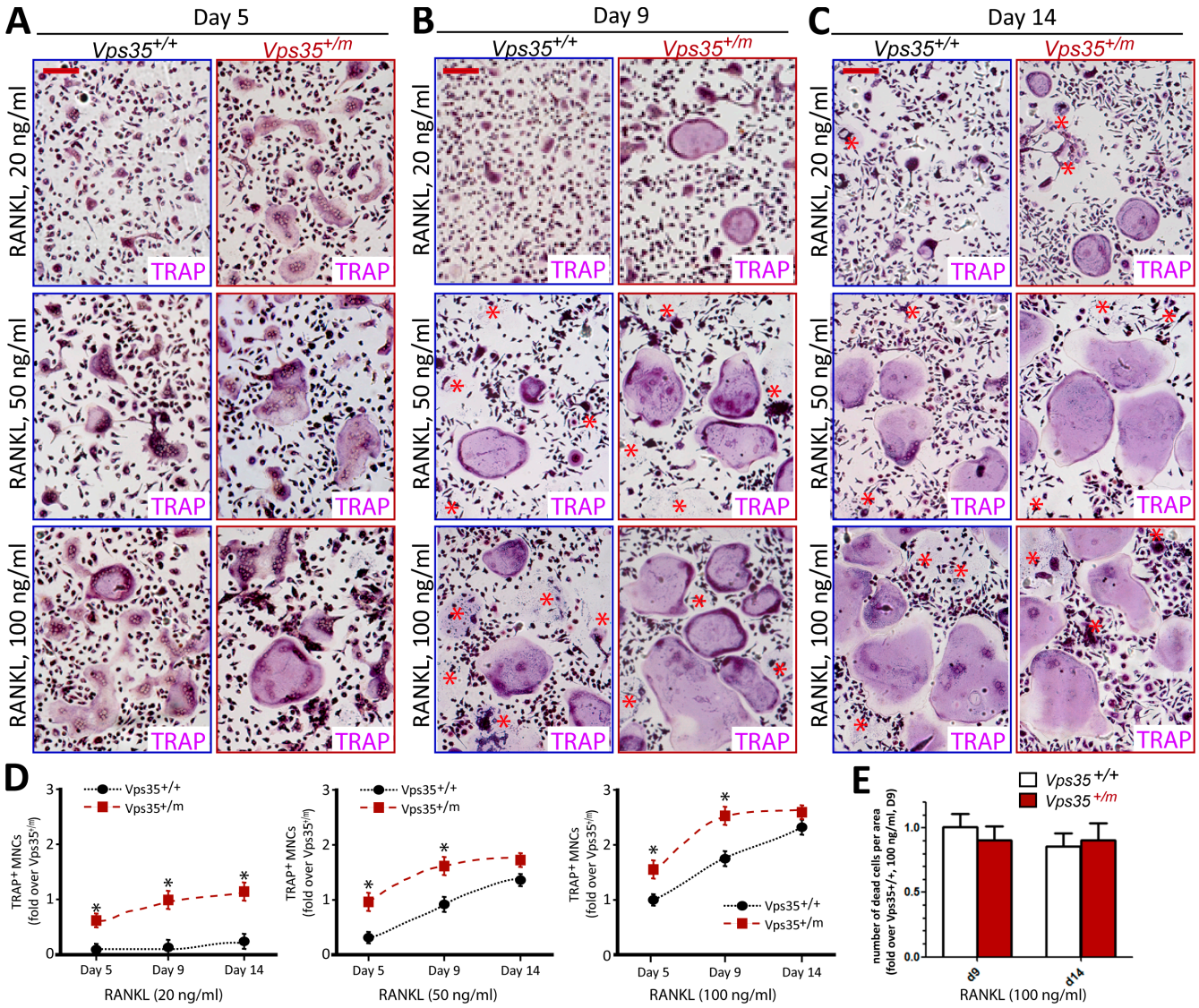

Figure 6. **Hypersensitivity to RANKL in Vps35$^{+/m}$ BMM culture.** TRAP staining analysis of OCs generated from BMMs of 1-mo-old Vps35$^{+/+}$ and Vps35$^{+/m}$ mice in the presence of 10% M-CSF and indicated concentrations of RANKL for 5, 9, and 14 d. Representative images were shown in A–C. The asterisks indicated the dead TRAP^{+} multinuclei cells. Quantitative analyses of the mean TRAP^{+} multinuclei (greater than three) cell (MNC) numbers per unit area and TRAP^{+} multinuclei cell death numbers per unit area are presented in D and E, respectively. The values of means ± SD from three different cultures during in vitro osteoclastogenesis are shown. *, $P < 0.05$, significant difference from WT control. Bars, 200 µm. Note that RANKL at a concentration as low as 20 ng/ml was able to induce OC formation in the mutant, but not in WT, culture, demonstrating hypersensitivity to RANKL.

Raw264.7 cells. In control Raw264.7 cells, the phosphorylation of IκB-α, Erk1/2, and Akt were only transiently detected at 5, 15, or 30 min, respectively, after RANKL stimulation (Fig. 7, A–D; and Fig. S3). However, in Vps35-depleted cells, these RANKL-induced phosphorylation events were increased in 5 or 15 min of stimulation and remained at high levels 60 min after the stimulation (Fig. 7, A–C; and Fig. S3). We next asked whether Vps35$^{+/m}$ BMMs behave as that of Vps35-deficient Raw264.7 cells. Yes, marked sustained increases of RANKL-induced phosphorylations of Erk1/2, Akt, and IκB-α were also detected in Vps35$^{+/m}$ BMM culture as compared with that of Vps35$^{+/+}$ BMMs (Fig. 7 E). No change of the total protein levels of Erk and Akt was detected in Vps35-deficient Raw264.7 or Vps35$^{+/m}$ BMMs (Fig. 7, A and E). Together, these results suggest that VPS35 prevents sustained RANK activation or signaling in both primary BMMs and Raw264.7 cells, identifying a potential mechanism underlying VPS35 suppression of hyperresorptive OC formation.

In B, D, and F, the values of means ± SD from three to five separate cultures are shown. (G and H) Increased secretion of cathepsins D and K in Vps35$^{+/m}$ OC culture was also detected by Western blot analysis. Lysates and medium of Vps35$^{+/+}$ and Vps35$^{+/m}$ OC culture (day 4–5 after RANKL incubation) were collected and subjected to Western blot analysis using the indicated antibodies (G). The levels of medium cathepsin D (Cath D) and K (Cath K) were quantified by ImageJ software, normalized with the control, and presented in H (means ± SD from three different cultures). *, $P < 0.05$, significant difference from WT control (ctrl). IB, immunoblot.

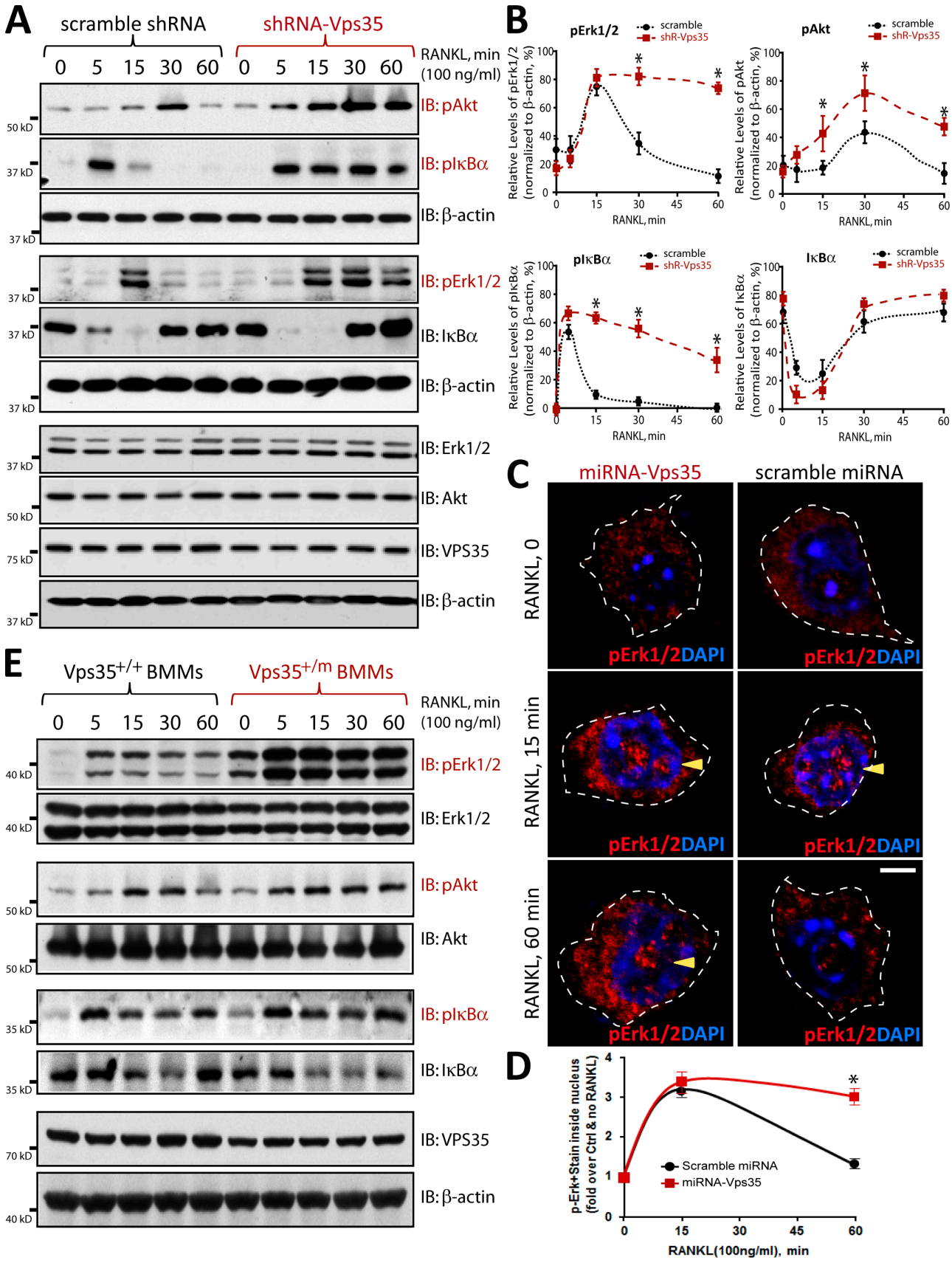

Figure 7. **Sustained RANKL-driven signaling in Vps35-deficient Raw264.7 cells and Vps35$^{+/m}$ BMMs.** (A and B) Sustained RANKL-driven signaling in Vps35-depleted Raw264.7 cells was revealed by Western blot analysis of lysates stimulated with RANKL for the indicated time. The data were quantified by ImageJ software and presented in B. The values of means ± SD from three separate experiments are shown. (C and D) Sustained RANKL-induced phosphorylation of Erk1/2 (pErk1/2) in Vps35-deficient Raw264.7 cells was revealed by immunostaining analysis with anti-pErk1/2 antibodies.

Defective endosome to Golgi translocation of RANK in Vps35-deficient Raw264.7 cells and Vps35$^{+/m}$ BMMs

To understand how VPS35 negatively regulate RANKL signaling, we asked whether VPS35 regulates RANK receptor trafficking. To this end, we first examined exogenous and endogenous RANK receptor distribution in control and Vps35-depleted Raw264.7 cells. The exogenous RANK-mCherry expressed in control cells displayed a cluster or punctae distribution pattern, and small portions of RANK-mCherry were co-distributed with VPS35, GM130 (a marker for Golgi apparatus), or LAMP1 (a marker for late endosome and early lysosome; Fig. 8, A–C). In Vps35-depleted Raw264.7 cells, such a RANK-mCherry distribution pattern was altered, with a decrease of RANK localization at the Golgi apparatus but an increase of RANK colocalization with LAMP1 (Fig. 8, A–C). An increased RANK-mCherry-EEA1 (an early endosome marker) colocalization was also detected in Vps35-depleted NLT (a gonadotropin-releasing hormone neuroblastoma cell line) cells (Fig. 8 D). These results suggest that a fraction of exogenous RANK may undergo endosome to Golgi translocation in a Vps35-dependent manner (Fig. 8 E). This view was next tested by coimmunostaining analysis of endogenous RANK in control and Vps35-deficient Raw264.7 cells. The anti-RANK antibody appeared to be specific, as it selectively recognized a major band (~80 kD) for endogenous RANK and two bands (120–130 kD) for exogenous RANK-mCherry proteins (Fig. S4, A and B). The endogenous RANK was largely distributed at the cell periphery of control Raw264.7 cells (Fig. 9 A), a different pattern from that of RANK-mCherry. Upon exposure to RANKL, RANK signal at intracellular and perinuclear organelles was detected, which we determined to be the Golgi apparatus by colocalization with the Golgi marker GRASP or GM130 (Fig. 9 B and not depicted). This RANKL-induced RANK translocation to the Golgi apparatus was abolished in Vps35-depleted Raw264.7 cells (Fig. 9, B–D). RANK association with endosomes (labeled by LAMP1 or EEA1) was increased in Vps35-depleted Raw264.7 cells (Fig. 9, E and F; and Fig. S4, C and D). These results support the view for Vps35/retromer in mediating RANKL-induced endosome to Golgi trafficking of RANK, implicating RANK as a cargo of VPS35/retromer.

Note that in addition to the defective RANK trafficking, the cell periphery immunofluorescence signal for endogenous RANK was increased in Vps35-depleted Raw264.7 cells (Fig. 9 G), suggesting an increase of RANK protein levels likely at the cell surface. This view was further confirmed by FACS analysis using phycoerythrin (PE)-conjugated RANK antibodies, which showed a significant increase of cell surface PE-labeled RANK in Vps35-depleted Raw264.7 cells (Fig. 9, H and I).

We second examined RANK distribution in Golgi apparatus in Vps35$^{+/+}$ and Vsp35$^{+/m}$ BMMs by biochemical iodixanol gradient fractionation assays, which separate early endosomes or cytosol vesicles from Golgi apparatus. In Vps35$^{+/+}$ and Vps35$^{+/m}$ BMMs, RANKL had no obvious effect on the distribution of GM130-or LAMP1-containing Golgi apparatus or lysosomes, based on their distributions in the fractionations isolated by iodixanol gradient centrifugation (Fig. 10, A and B; and not depicted). However, RANKL increased RANK distribution in fractions enriched with Golgi apparatus in Vps35$^{+/+}$, but not Vps35$^{+/m}$, BMMs (Fig. 10, A–C). These results thus provide additional support for VPS35-dependent Golgi translocation of RANK in macrophages. Interestingly, VPS35's distribution was also shifted from EEA1^{+} to GM130/LAMP1^{+} fractions in RANKL-stimulated Vps35$^{+/+}$, but not Vps35$^{+/m}$, BMMs (Fig. 10 B). Thus, we speculate that RANKL may increase RANK and VPS35 association. This view was in line with the results of coimmunostaining analysis of the endogenous RANK and VPS35 in Raw264.7 cells stimulated with or without RANKL (Fig. 10, D and E). In which, RANKL increased RANK-VPS35 colocalization in a time-dependent manner (Fig. 10, D and E). The time course was similar to that of RANKL-induced RANK translocation to the Golgi apparatus as well as termination of RANK signaling in Raw264.7 cells (Fig. 7 and Fig. 9). Collectively, these results suggest that upon RANKL stimulation, RANK may interact with VPS35/retromer, resulting in their endosome to Golgi/lysosome translocation and inactivation of RANK signaling.

Increased RANK protein levels in Vps35-depleted Raw264.7 cells but not Vps35$^{+/m}$ BMMs

We further examined properties or mechanisms of the increased RANK cell surface levels in Vps35-deficient Raw264.7 cells (Fig. 9, G–I), with an attempt to address whether such increase of RANK contributes to the increased or sustained RANKL signaling (Fig. 7). First, the increased cell surface levels of RANK in Vps35-deficient Raw264.7 cells correlated well with the increase of total RANK protein levels detected by Western blot analysis (Fig. S5 A). Second, this effect appeared to be RANK selective, as no change of protein levels of TREM2, receptor for advanced glycation end products (RAGE), and CD40, other membrane receptors important for OC genesis (e.g., c-Fms [a receptor for M-CSF], TREM2, and RAGE; Paloneva et al., 2003; Zhou et al., 2006), was detected in Vps35-deficient Raw264.7 cells (Fig. S5 A). A slight increase of c-Fms, a receptor for M-CSF, was observed in the Vps35-deficient Raw264.7 cells (Fig. S5 A), suggesting that RANK may not be the only receptor affected by Vps35 depletion. Third, the increases of RANK and

The immunofluorescence signals in the nuclei (indicated by the arrowheads) over that in the cytoplasm were quantified and presented in D. The means ± SD from three different cultures with total of 50 cells were shown. Bars, 10 µm. Note that upon RANKL stimulation for 1 h, pErk1/2 signals at the nuclei of Raw264.7 cells were significantly reduced in the control, but not Vps35-depleted, culture. The dotted lines indicate the borders of the cell. (E) Sustained RANKL-induced signaling was also observed in BMMs derived from Vps35$^{+/m}$ mice. Note that RANKL-induced pErk1/2 and pAkt signals were markedly increased and sustained in Vps35 mutant BMMs, in line with that of the Vps35-depleted Raw264.7 cells. IB, immunoblot. *, $P < 0.05$, significant difference from scramble control (Crtl).

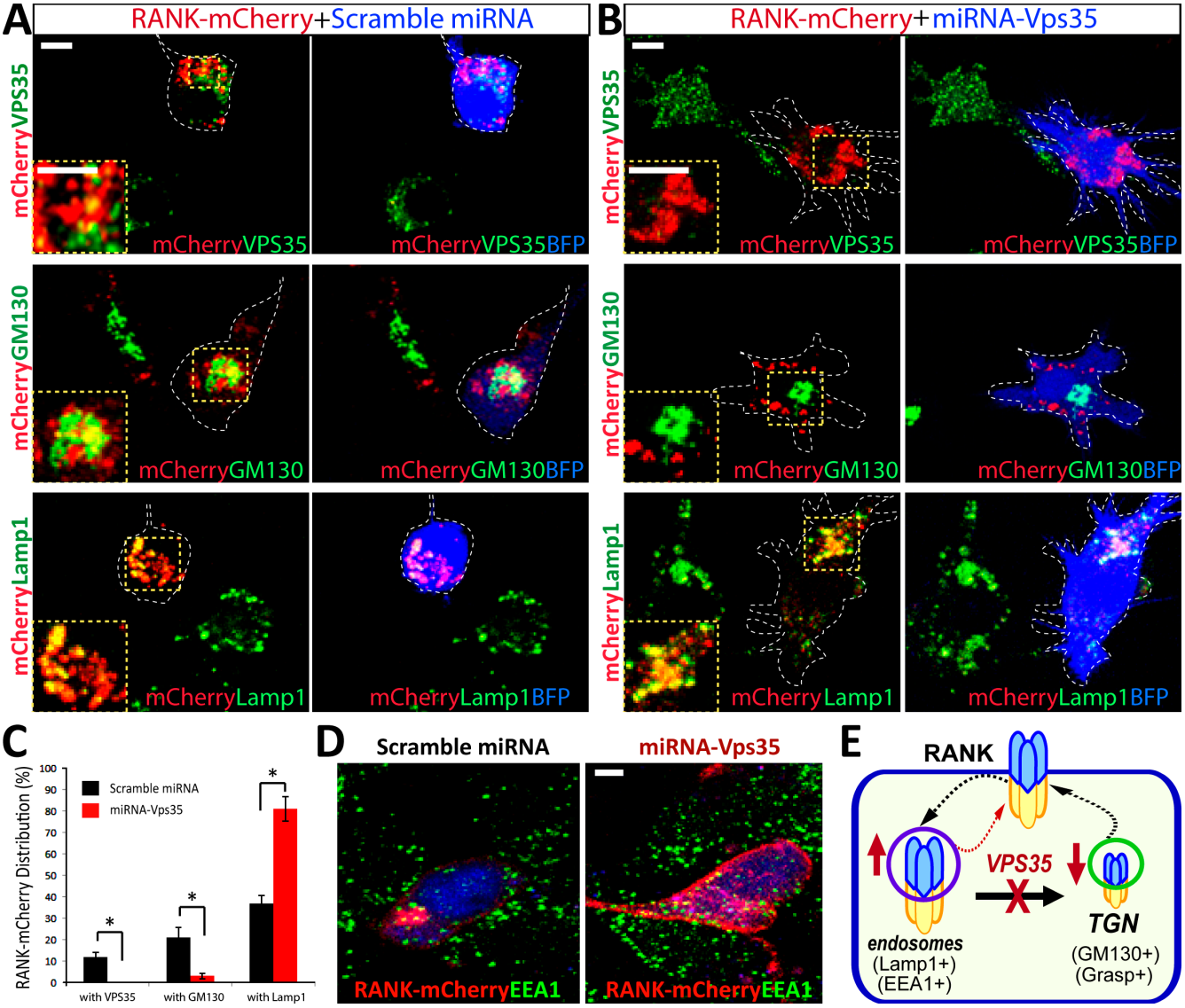

Figure 8. **Altered exogenous RANK distribution in Vps35-deficient cells.** (A and B) Coimmunostaining analysis of exogenous RANK with endogenous VPS35, GM130, and LAMP1 in Raw264.7 cells transfected with RANK-mCherry with control (A) or shRNA-Vps35 (B). Images marked with yellow squares are amplified and shown in the left corners. The dotted lines indicate the BFP-expressing cell. (C) Quantification analysis of data from A and B using ImageJ. The colocalization index of RANK with indicated markers (VPS35, GM130, and LAMP1) was determined by the measurement of overlapped signal (yellow fluorescence) over total RANK-mCherry signal. Data were shown as means ± SD (n = 20). *, $P < 0.01$, compared with control shRNA cells. (D) Coimmunostaining analysis of exogenous RANK with endogenous EEA1 (an early endosome marker) in NLT cells (gonadotropin-releasing hormone neuroblastoma cells) transfected with RANK-mCherry with control or miRNA-Vps35. Note that increased RANK colocalization with EEA1 and cell surface levels were observed in Vps35-depleted NLT cells. (E) A schematic illustration of VPS35 regulating RANK trafficking. Bar, 10 µm.

c-Fms proteins were not detected in Vps35$^{+/m}$ BMMs; instead, a slight reduction of RANK was observed in Vps35$^{+/m}$ BMMs (Fig. S5 B). These results thus suggest that VPS35 selectively regulates membrane protein levels (or degradation) in a cell type/stage–dependent manner. Fourth, the increase of RANK levels in Vps35-deficient Raw264.7 cells appeared to be caused in a large part by an impaired RANK degradation (Fig. S5, C–E). Finally, VPS35 regulation of RANK protein levels was RANKL independent, as the total levels of RANK and RANK degradation were unaffected by RANKL stimulation (Fig. S5, F and G; and not depicted). Collectively, these results suggest that VPS35 may regulate RANK degradation and control RANK protein levels in a cell type/stage–specific manner.

Discussion

Although the signaling and function of RANK have been studied extensively, there is increasing emphasis toward our understanding of how RANK signaling is negatively regulated to restrain OC differentiation in a physiological condition. Here, we provide evidence for VPS35, a major component of the retromer, in negatively regulating RANK signaling and function. Based on our results, we proposed that VPS35/retromer deficiency in OC lineage cells results in defective RANK endosome to Golgi trafficking, enhanced RANKL signaling, increased hyperresorptive OC formation, and osteoporotic deficit.

OCs are generated by the differentiation of monocyte/macrophage precursors at the bone surface. Close contact

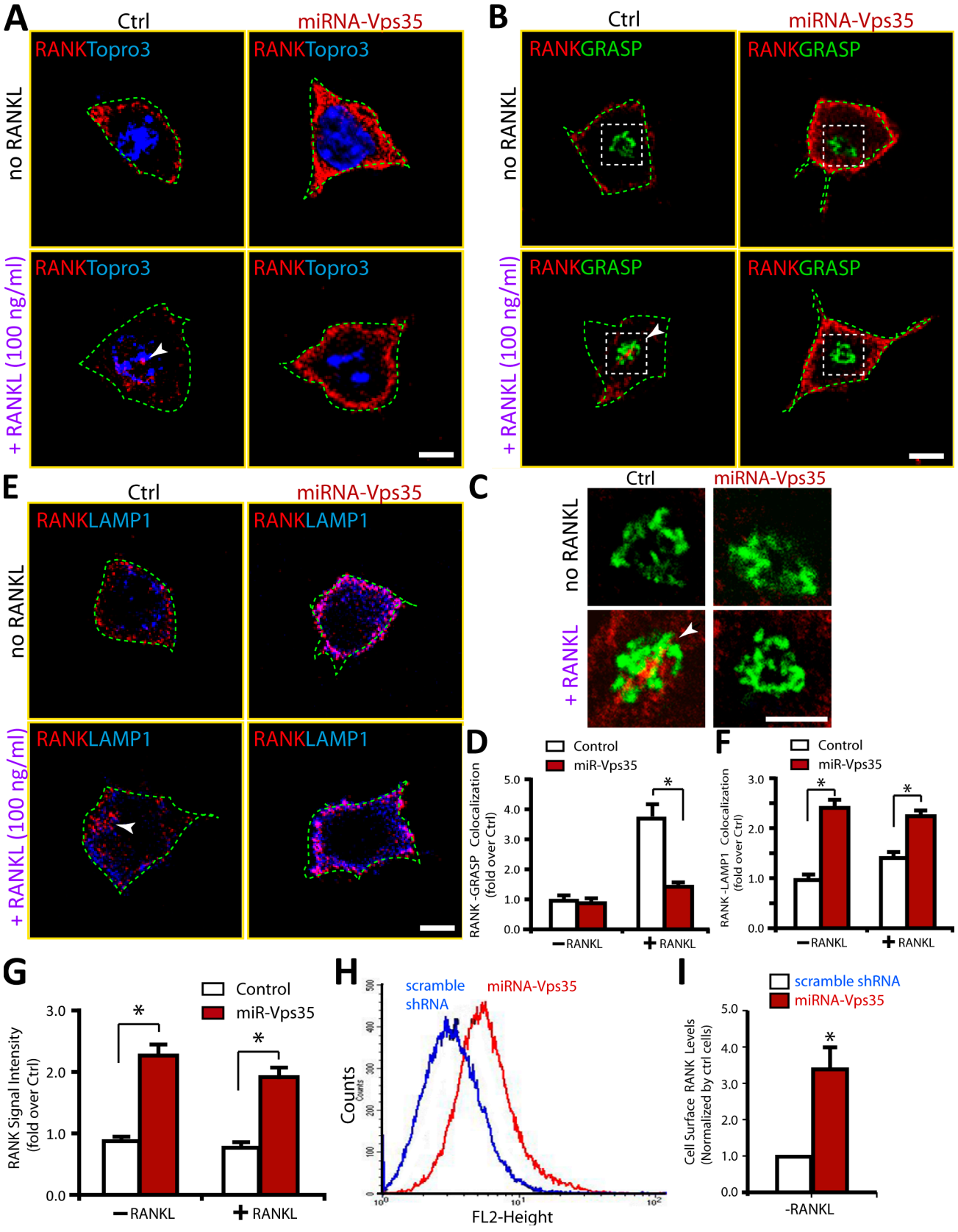

Figure 9. **Impaired RANKL-induced endosome to Golgi translocation of endogenous RANK and increased cell surface levels of RANK in Vps35-deficient Raw264.7 cells.** (A–F) An impaired RANKL-induced endosome to Golgi translocation of RANK in Raw264.7 cells expressing miRNA-Vps35 was revealed by coimmunostaining analyses using the indicated antibodies. Confocal representative images are shown in A–C and E. Images marked with white squares in B were amplified and shown in C. Bars, 10 µm. The quantitative analysis of RANK translocation to TGN in the percentage of miRNA-expressing cells (normalized by control cells) is shown in D (means ± SD, *n* = 30). The quantitative analysis of RANK-LAMP1 colocalization signal over total RANK in

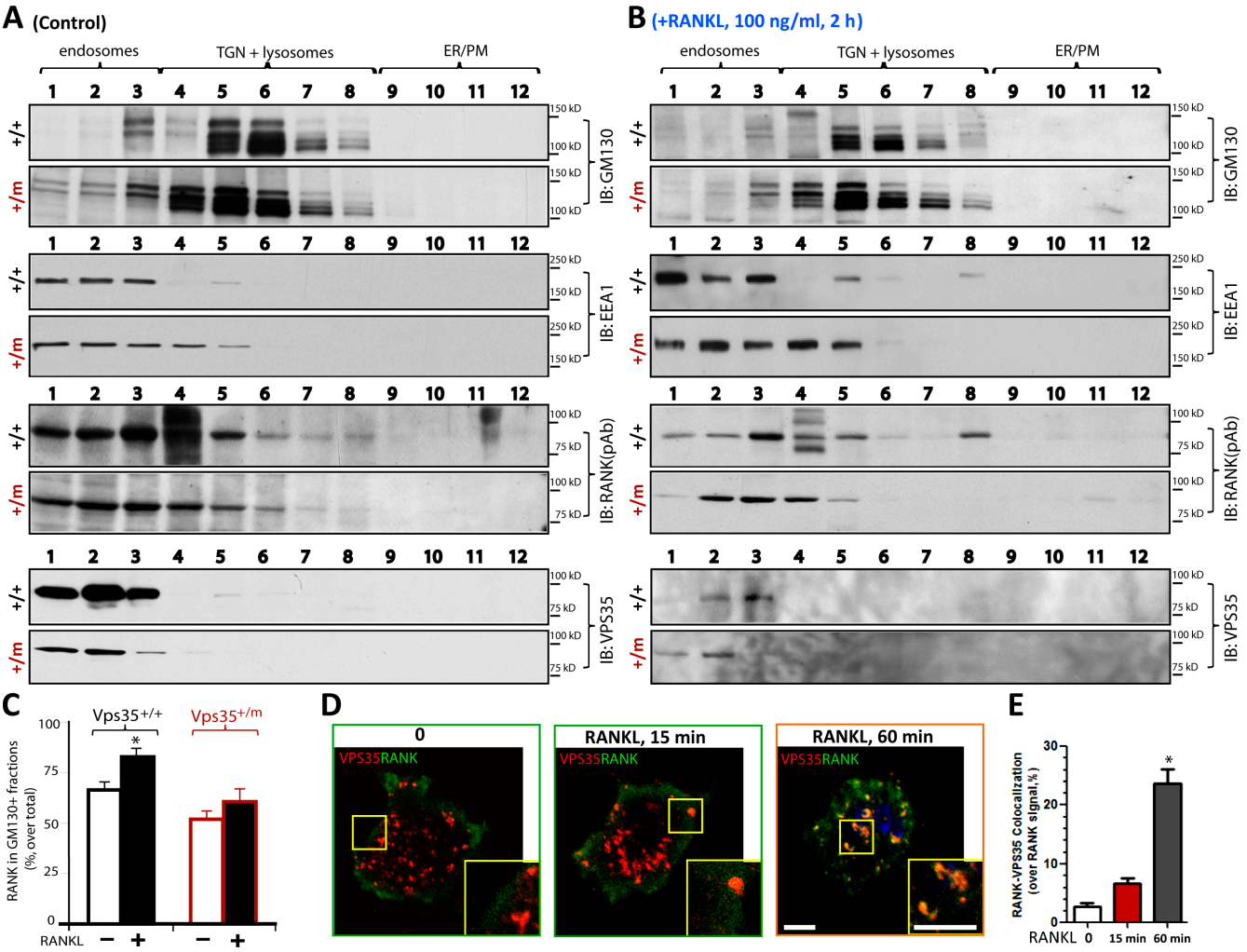

Figure 10. **RANKL-induced RANK distribution in Golgi apparatus in Vps35$^{+/+}$, but not Vps35$^{+/m}$, BMMs.** (A–C) Western blot analyses of RANK distribution in different subcellular fractions collected after iodixanol gradient centrifugation of Vps35$^{+/+}$ and Vps35$^{+/m}$ BMMs stimulated with control (A) or 100 ng/ml RANKL (2 h; B). 12 fractions were collected after iodixanol gradient centrifugation (see Materials and methods). Data in A and B were quantified and presented as the percentage of total RANK in C (means ± SD, n = 3). RANK in GM130^{+} Golgi fractions was increased in Vps35$^{+/+}$, but not Vps35$^{+/m}$, BMMs after RANKL stimulation. Note that basal levels of RANK in GM130^{+} Golgi fractions of BMMs appeared to be higher than that in Raw264.7 cells detected by coimmunostaining analysis (see Fig. 9). This may be caused by the difference of the cells and/or detection methods. IB, immunoblot; PM, plasma membrane. (D and E) Coimmunostaining analysis of RANK with VPS35 in Raw264.7 cells stimulated with 100 ng/ml RANKL for the indicated time. Representative images are shown in D, and quantification analysis of RANK-VPS35 colocalization signal over total RANK is shown in E. Images marked with yellow boxes are amplified and shown in the right corners. The values of means ± SD, n = 30 cells per group, are shown. *, P < 0.01, in comparison to the control (no RANKL). Bars, 10 µm.

between mesenchymal stem cells and BMMs within basic multicellular units is essential for osteoclastogenesis in vivo, as mesenchymal stem cell–derived factors, M-CSF and RANKL, activate receptors on BMMs, thereby stimulating OC differentiation (Boyle et al., 2003; Teitelbaum and Ross, 2003). Although M-CSF is essential for the proliferation and survival of osteoclastic precursors, RANKL is the unique osteoclastogenesis cytokine promoting OC formation (Boyle et al., 2003; Teitelbaum and Ross, 2003; Novack, 2011). Given the importance of the RANKL–RANK pathway in OC formation, we assessed the role of RANK in Vps35 depletion–induced hyperresorptive osteoclastogenesis. Indeed, RANK's contribution to the phenotype is revealed by the hypersensitivity to RANKL, sustained RANKL signaling, and increased RANKL-induced

miRNA-expressing cells (normalized by control cells) is shown in F (means ± SD, n = 30). *, P < 0.01, compared with control miRNA cells. The arrowheads indicate the colocalizations. The green dotted lines indicate the borders of the cells. (G–I) Increased RANK cell surface levels in Vps35-depleted Raw264.7 cells were revealed by quantitative analysis of RANK cell surface signal by immunostaining (G) and FACS (H and I) analyses. In G, the means ± SD (n = 30) are presented. *, P < 0.05, significant difference from control. In H, control and shRNA-Vps35–expressing Raw264.7 cells were incubated with PE-conjugated anti-RANK antibodies for 30 min. Cells were then subjected to flow cytometric analysis (see Materials and methods). In I, the cell surface levels (means ± SD, n = 3) of RANK detected by FACS analysis were presented. *, P < 0.05, significant difference from control. Ctrl, control.

OC genesis in Vps35-depleted macrophages (Fig. 6, Fig. 7, Fig. 8, and Fig. 9). Our results are also in line with the view that sustained RANKL signaling is critical for OC formation and activation (Novack, 2011).

Further mechanistic experiments suggest that RANK appears to be a novel cargo of VPS35/retromer (Fig. 8, Fig. 9, and Fig. 10). VPS35-mediated RANK endosome to Golgi translocation was increased by RANKL stimulation as well as by RANK overexpression, both events inducing RANK oligomerization or aggregation. We thus speculate that RANK oligomer may be a better cargo for VPS35/retromer, in which, RANK activation or oligomerization may increase its association with VPS35, therefore undergoing endosome to Golgi translocation. Such translocation may be critical for turning off RANK signaling or inactivating RANK. This view is in line with a recent study that retromer terminates parathyroid hormone–induced increase of cAMP by interacting with PTH1R and promoting its translocation to TGN in HEK 293T cells (Feinstein et al., 2011). Together, these observations suggest that VPS35/retromer-mediated endosome to Golgi trafficking of receptors may be a mechanism for turning off signaling initiated by transmembrane receptors. However, it is also possible that VPS35/retromer regulates endosome to lysosome trafficking of receptors, which terminates the receptor signaling. Both possibilities require further investigations.

Although our studies suggest that RANK appears to be the VPS35/retromer cargo responsible for Vps35 deficiency–induced OC genesis, it may not be the only one. Increased levels of c-Fms, a receptor for M-CSF, were detected in Vps35-deficient Raw264.7 cells. But, the increases of RANK and c-Fms were not detected in $Vps35^{+/m}$ BMMs (Fig. S5), suggesting a cell type/stage dependency of VPS35's function in promoting RANK and c-Fms protein degradation. Also noteworthy is that TREM2 and RAGE, other receptors critical for OC genesis (Paloneva et al., 2003; Zhou et al., 2006), were unaffected by Vps35 suppression in Raw264.7 and BMMs (Fig. S5, A and B). These results thus support the view that VPS35/retromer selectively regulates membrane protein/receptor degradation in a cell type/stage–dependent manner. The function of VPS35 regulation of RANK degradation during OC genesis and activation needs to be investigated.

The increased OCs in $Vps35^{+/m}$ mice may reflect more robust differentiation of BMMs into mature OCs. But, it remains to be determined whether enhanced precursor/progenitor proliferation and/or reduced OC apoptosis also contribute to the increased OCs. Although our observations have pointed to the importance of hyperresorptive OCs for the osteoporotic deficit in Vps35 mutant mice, the reduced bone formation may also have a critical role in this deficit. In fact, a reduction of endocortical bone formation in Vps35 mutant mice was observed (Fig. 3). However, mechanisms underlying VPS35 promoting bone formation appear to be a complex. The decreased endocortical bone formation in Vps35 mutant mice may be caused by impaired Wntless trafficking and secretion of Wnts, a family of important extracellular morphogens that regulates bone remodeling and bone formation (Kubota et al., 2009; Guo et al., 2010), and/or an altered PTH1R's trafficking and signaling in Vps35-deficient OBs. Further investigations are necessary to address the underlying mechanisms.

Collectively, the data presented in this manuscript demonstrate an unrecognized function of VPS35 in regulating RANK trafficking. This event appears to be critical for turning off RANK signaling and preventing RANK-mediated hyperresorptive OC formation and activation.

Materials and methods

Reagents and animals

Rabbit polyclonal anti-VPS35 antibody was generated using the antigen of GST-VPS35D1 fusion protein as described previously (Wen et al., 2011). Rabbit polyclonal antibodies, including anti-RANK (Cell Signaling Technology), anti-GRASP65 (Abcam), antiphospho-Akt (Cell Signaling Technology), antiphospho–IκB-α (Cell Signaling Technology), and antiphospho-Erk1/2 (Cell Signaling Technology) antibodies, mouse monoclonal antibodies, including anti-RANK (Abcam), anti–IκB-α (Cell Signaling Technology), and anti-GM130 (BD) antibodies, and rat anti-Lamp1 (Developmental Studies Hybridoma Bank) and anti-Lamp2 (Developmental Studies Hybridoma Bank) antibodies were used. In addition, Alexa Fluor 488 phalloidin (Invitrogen) was used to visualize F-actin filaments. Secondary antibodies were purchased from Jackson ImmunoResearch Laboratories, Inc. Murine M-CSF was obtained from R&D Systems. Recombinant GST-RANKL protein were generated and purified as previously described (Zhou et al., 2006, 2008; Cui et al., 2011). Other chemicals and reagents used in this study were of analytical grade.

Vps35 mutant mice were generated by injection of mutant embryonic stem cells obtained from BayGenomics as described previously (Wen et al., 2011). In brief, embryonic stem cells containing a gene-trapping vector that disrupts the Vps35 gene were transferred into mouse blastocysts. The mutant Vps35 gene was identified by PCR genotyping using three primers (5′-GGCCACCAACAGATTGGGAAAGG-3′, 5′-AGCAATGGAGGAGTGTTCCTCTTTC-3′, and 5′-CACTCCAACCTCCGCAAACTC-3′). Chimeras were crossed to C57BL/6J mice for more than F6 generations. Mice were maintained on a standard rodent diet (Tekled S-2335; Harlan). Control littermates ($Vps35^{+/+}$ and $Vps35^{+/m}$) were processed in parallel for each experiment. The Vps35 mutation was confirmed by genotyping using PCRs and by Western blot analysis as described previously (Wen et al., 2011). All experimental procedures were approved by the Animal Subjects Committee at the Georgia Health Sciences University according to US National Institutes of Health guidelines.

Plasmids encoding miRNA-Vps35 and RANK-mCherry and lentivirus encoding shRNA-Vps35

The miRNA-Vps35 expression vector was generated by the lentiviral miRNA expression system (BLOCK-iT; Invitrogen) according to the manufacturer's instruction as previously described (Zhu et al., 2007; Wen et al., 2011; Liu et al., 2012). The target sequences, 5′-AGGTGTAAATGTGGAACGTTA-3′ (for miRNA-Vps35) and 5′-GGTACATCTATTTCTATGAAA-3′ (for shRNA), were designed using web-based Block-iT program (Invitrogen) and subcloned into pcDNA 6.2-GW/emerald GFP–miRNA (Invitrogen) and pLV-shRNA (Biosettia) vectors, respectively. The RANK-mCherry expression plasmid was generated by fusion of the mCherry to the C terminus of the RT-PCR amplified mouse RANK in a mammalian expression vector under control of the CAG promoter. The authenticity of all constructs was verified by DNA sequencing.

The lentivirus was packaged by cotransfection of pLV-shRNA-Vps35 with virus packaging plasmids into HEK (human embryonic kidney) 293T cells using the calcium phosphate method as described previously (Chen et al., 2010b; Xiong et al., 2011a). In brief, 15 µg DNA mixture (7.5 µg pLV-shRNA-Vps35 and 7.5 µg pVSVG, PLP1, and PLP2, each at 2.5 µg, for one 100-mm dish) were prepared in 250 mM $CaCl_2$ solutions, which were then mixed with 2× HeBS (274 mM NaCl, 10 mM KCl, 1.4 mM Na_2HPO_4, 15 mM glucose, and 42 mM Hepes) drop by drop to make the transfection mixture. The transfection mixture was incubated with 293FT cells for ∼60 min and stopped by aspirating the transfection medium and washing cells with fresh medium. 48 h after transfection, the viral supernatants were harvested and concentrated by centrifugation (25,000 rpm for 90 min at 4°).

β-Gal detection, immunofluorescence staining, and confocal imaging analysis

β-Gal activity was detected as described previously (Lee et al., 2010; Zhou et al., 2010; Wen et al., 2011). In brief, frozen femur sections and

freshly isolated BMSCs or BMMs derived from neonatal mice ($Vps35^{+/+}$ and $Vps35^{+/m}$) were fixed with 0.5% glutaraldehyde and incubated with X-gal solution (2 mM $MgCl_2$, 5 mM potassium ferricyanide, 5 mM potassium ferrocyanide, and 0.1% X-gal) in the dark at 37°C for 8 h. The slides were washed, mounted in Permount (Thermo Fisher Scientific), and imaged using deconvolution digital microscope (Axioplan 2; Carl Zeiss) with high sensitivity camera (AxioCam; Carl Zeiss) and equipped with a Plan-Neofluar 5× and Plan-Neofluar 10×/0.30 NA objective lens.

For immunofluorescence staining analysis, primary OCs or Raw264.7 cells plated onto coverslips were fixed with 4% paraformaldehyde and 4% sucrose at room temperature for 15 min, permeabilized in 0.15% Triton X-100 for 8 min, and then subjected to coimmunostaining analysis using the indicated antibodies. The stained cells were washed three times with PBS and mounted with VECTASHIELD (Vector Laboratories) for imaging analysis by upright confocal microscope (LSM 510; Carl Zeiss) with 405-, 488-, 561-, and 633-nm lasers (LSM 510 software; Carl Zeiss) at room temperature. A Plan-Apochromat 63×/1.40 NA oil differential interference contrast M27 objective or an EC Plan-Neofluar 40×/1.30 NA oil differential interference contrast M27 objective lens (Carl Zeiss) was used with immersion oil (Immersol 518N; Carl Zeiss). The acquired 8-bit RGB images were exported to .TIFF files with the LSM 510 viewer software. Photoshop software CS5 (Adobe) was used to adjust the brightness. Figures were constructed in Illustrator version CS5 (Adobe). For fluorescent quantification, morphometric measurements of images were performed using ImageJ software (National Institutes of Health).

Cell culture and transient transfection

Raw264.7 cells were maintained in DMEM supplemented with 10% fetal calf serum and 100 U/ml of penicillin G and streptomycin (Gibco). For transfection, Raw264.7 cells were plated at a density of 10^6 cells per 10-cm culture dish and allowed to grow for 12 h before transfection using Lipofectamine 2000 (Invitrogen). 48 h after transfection, cells were subjected to immunostaining analysis.

μCT

Microarchitecture of the distal trabecular bone and midshaft cortical bone of the femur were measured by μCT 40 (Scanco Medical). Bones were placed vertically in 12-mm-diameter scanning holders and scanned at the following settings: 12-μm resolution, 55-kVp energy, 145-μA intensity, and an integration time of 200 ms.

The scan of the trabecular bone was performed from the growth plate and consisted of 200 slices (each slice was 12 μm in thickness). Scans were automatically reconstructed into 2D slices, and 100 slices were analyzed using the μCT Evaluation Program (v5.0A; Scanco Medical). The region of interest (ROI) was drawn on each of the 100 slices just inside the cortical bone to include only the trabecular bone and marrow. Trabecular bone was thresholded at 245, to distinguish it from the marrow. The 3D reconstruction was performed using all the outlined slices. No cortical bone was included in this analysis. Data were obtained on BV, total volume (TV), BV/TV, bone density, trabecular number, and connectivity.

The scan of the cortical bone was performed at the midshaft of the femur and consisted of 25 slices (each slice was 12 μm in thickness). Fewer slices were needed for the cortical scan, as the cortical bone at the midshaft is very uniform. Scans were reconstructed as for the trabecular scans, and the ROI was drawn on all 25 slices. For the cortical scan, the ROI was drawn at the outside of the cortical bone and included all the cortical bone and marrow. There was no trabecular bone in these images at the midshaft. Cortical bone was thresholded at 329, and the 3D reconstruction was performed on all 25 slices. Data were obtained on BV, TV, BV/TV, bone density, and cortical thickness.

Complete femur was scanned under the following setting to get entire femur 3D images: bones were placed in a horizontal position in 20-mm-diameter scanning holders and scanned at 20-μm resolution, 70-kVp energy, 114-μA intensity, and an integration time of 200 ms. The ROI was drawn at the outside of the cortical bone and included all the cortical bone and marrow, and the bone was thresholded at 245.

Bone histomorphometric analysis

Bone histomorphometric analyses were performed as previously described (Zhou et al., 2006, 2008; Cui et al., 2011). In brief, mouse tibia and femurs were fixed overnight in 10% buffered formalin, decalcified in 14% EDTA, embedded in paraffin, sectioned, and subjected for hematoxylin and eosin, safranin O, and TRAP staining analyses, which were counterstained by fast green. Bone histomorphometric perimeters were determined by measuring the areas situated ≥0.5 mm from the growth plate, excluding the primary spongiosa and trabeculae connected to the cortical bone.

Measurements of serum levels of osteocalcin, PYD, and IL-6

Mouse serum samples were collected and subjected to RIA analysis of PYD and ELISA analyses of IL-6 and osteocalcin as described previously (Zhou et al., 2006; Cui et al., 2011). Metra serum PYD RIA kit (Quidel Corporation), mouse IL-6 ELISA kit (BD), and mouse osteocalcin ELISA kit (Biomedical Technologies, Inc.) were used. All the samples were measured in duplicate, and values were subjected to statistical analysis. For measurement of PYD, 25-μl serum samples were incubated with 75 μl PYD antibody solution overnight at 4°C in the dark. After three washes, samples were incubated with enzyme conjugates for 60 min at room temperature and followed by three washes and incubation with 150 μl substrate solution at room temperature for 40 min. The reaction was stopped, and the OD measured at 405 nm was converted to PYD concentrations using a standard curve. For measurement of IL-6, 50-μl serum samples with 50 μl ELISA diluent were incubated for 2 h at room temperature. After five washes, samples were incubated with 100 μl of working detector for 1 h at room temperature followed by seven washes and incubation with 100 μl of 3,3′-5,5′ tetramethylbenzidine One-Step Substrate Reagent (30 min at room temperature). The reaction was stopped, and the OD measured at 450 nm within 30 min of stopping reaction was then converted to IL-6 concentrations using a standard curve. For mouse serum levels of osteocalcin, it was measured at 1:5 dilutions of collected serum samples. Serum samples (25-μl diluted samples) were incubated at 4°C overnight with 100 μl biotin–mouse osteocalcin antibody. After three washes, 100 μl HRP–streptococcus A was added and incubated in the dark at room temperature for 30 min. 100 μl of 3,3′-5,5′ tetramethylbenzidine-Perox was then added after three washes to incubate for 15 min at room temperature. The reaction was stopped, and the OD was measured at 450 nm within 30 min of stopping reaction and then converted to osteocalcin concentrations using a standard curve.

Dynamic bone histomorphometry to measure the rate of bone formation in vivo

In brief, 2-wk-old mice were injected (intraperitoneally) with 10 mg/kg fluorochrome-labeled calcein green (Sigma-Aldrich) and then with 50 mg/kg alizarin red S (12-d interval; Sigma-Aldrich). The mice were sacrificed 2 d after the second injection. The left tibia and femurs were fixed in 70% ETOH overnight, embedded in methyl methacrylate, and sectioned at 7–10 μm. Images were obtained using a 25× objective fluorescence microscope (LSM 510). The MARs in micrometers per day and BFRs (BFR = MAR × mineral surface/bone surface) were calculated from fluorochrome double labels at the periosteal and endocortical surfaces.

In vitro OB culture

Whole bone marrow cells were isolated from long bones of 8-wk-old WT and $Vps35^{+/m}$ mice and plated on 100-mm tissue-culture plates in DMEM containing 10% FBS and 1% penicillin/streptomycin. After 7 d, passaging cells by trypsin digestion, $10^4/cm^2$ were plated for osteogenesis differentiation in the presence of osteogenic medium (DMEM containing 10% FBS, 1% penicillin/streptomycin,10 mM β-glycerophosphate, and 50 μM L-ascorbic acid-2-phosphate). After 14 d of incubation, ALP staining and quantification analyses were performed.

In vitro BMM and OC culture

Mouse BMMs and OCs were generated as described previously (Zhou et al., 2006; Cui et al., 2011). In brief, the bone marrow was flushed from femurs and tibiae of 6-wk-old WT and Vps35 mutant mice with ice-cold α-MEM and plated on 100-mm tissue-culture plates in α-MEM containing 10% FBS and 10 ng/ml recombinant M-CSF. Cells were incubated at 37°C with 5% CO_2 overnight. Nonadherent cells were harvested and subjected to Ficoll–Hypaque gradient centrifugation for purification of BMMs. For osteoclastogenesis culture, 5×10^4 BMMs were incubated with OC differentiation medium containing 10 ng/ml recombinant M-CSF and 100 ng/ml recombinant RANKL. Mature OC (multinucleated, large spread cells) began to form at day 4–5 after RANKL treatment. The cells were then subjected to TRAP staining to confirm their OC identity.

In vitro resorption assay of cultured OCs

BMMs plated in 16-well slides (BioCoat Osteologic MultiTest; BD), which are coated with inorganic hydroxyapatite matrix, were incubated with OC differentiation medium containing 10 ng/ml M-CSF and 100 ng/ml RANKL for 8 d. The culture medium was changed every other day. At day 8,

slides were washed with bleach (6% NaOCl and 5.2% NaCl) for 5 min to remove cells followed by three washes with distilled water. The slides were then stained with fresh 5% silver nitrate for 30 min, developed with fresh 5% sodium carbonate in 25% formalin, and fixed with 5% sodium thiosulphate for 2 min. The putative resorption pits (white area) were visualized by using a deconvolution digital microscope (Axioplan 2) with high sensitivity camera (AxioCam) and equipped with a Plan-Neofluar 5× and Plan-Neofluar 10×/0.30 NA objective lens. The data were analyzed using ImageJ software.

FACS

FACS was performed as described previously (Hildebrand et al., 2011). In brief, Raw264.7 cells infected with lentivirus of control shRNA and shRNA-Vps35 were incubated with PE-conjugated anti-RANK (BioLegend) for 30 min at 0°C. Flow cytometric analysis was performed using a flow cytometer (FACSCalibur; BD). Acquisition and analysis were performed using CellQuest Pro software (BD).

Iodixanol gradient centrifugation

The iodixanol gradient centrifugation assay was performed as described previously (Cai et al., 2006). In brief, BMMs derived from 1-mo-old $Vps35^{+/+}$ and $Vsp35^{+/m}$ mice were cultured in the presence of 10% M-CSF for 3–5 d. After 2-h incubation with or without 100 ng/ml RANKL, BMM cells were broken by five passes through a 26-gauge needle and homogenized by 50 strokes in a homogenizer in 1-ml homogenization buffer (0.25 m sucrose, 20 mm Tris-HCl, pH 7.4, 2 mm EGTA, and a protease inhibitor mixture). To remove nuclei-containing pellets, the homogenates were centrifuged for 10 min at 1,000 *g*, and the supernatants were then loaded on top of a continuous 5–25% iodixanol (OptiPrep Density Gradient Medium; Sigma-Aldrich), formed according to the manufacturer's protocol, and centrifuged for 2.5 h at 200,000 *g* in a rotor (SW 41 Ti; Beckman Coulter). 12 fractions (each at 1 ml) were collected from the bottom of each gradient. The protein in each fraction was then precipitated with trichloroacetic acid and washed twice with acetone. Precipitated proteins were resuspended in SDS sample buffer, resolved by SDS-PAGE, and subjected for Western blotting analyses.

Statistical analysis

All data were expressed as means ± SD. For in vivo experiments, five to six mice per genotype per assay were used. For in vitro cell biological and biochemical experiments, each experiment was repeated three times. 10–50 cells were quantified for immunostaining analyses. The significance level was set at $P < 0.05$, and the Student's *t* test was used.

Online supplemental material

Fig. S1 shows enzymatic LacZ activity in postnatal day 3 (P3) $Vps35^{+/m}$ femur and co-distribution of LacZ with TRAP-positive cells in P7 $Vps35^{+/m}$ femur. Fig. S2 shows suppression of Vps35 expression in Raw264.7 macrophages by lentivirus encoding shRNA-Vps35. Fig. S3 shows sustained RANKL-induced phosphorylation of IκB-α in Vps35-depleted macrophages. Fig. S4 shows RANK antibody specificity and RANK-EEA1 colocalization in Raw264.7 cells. Fig. S5 shows increased RANK protein levels and impaired RANK degradation in Vps35-depleted Raw264.7 cells but not $Vps35^{+/m}$ BMMs. Online supplemental material is available at http://www.jcb.org/cgi/content/full/jcb.201207154/DC1.

We thank members of Drs. Xiong and Mei laboratories and Dr. X.M. Shi (Georgia Health Sciences University) for helpful discussions and suggestions. We thank the Medical College of Georgia histomorphological core for cutting mouse femur and tibia bone sections, Medical College of Georgia imaging core for providing instrumentations, and The University of Alabama μCT core for μCT analyses.

This work was supported in part by grants from the National Institutes of Health (to W.-C. Xiong and L. Mei) and Veterans Administration (BX000838 to W.-C. Xiong).

Submitted: 24 July 2012
Accepted: 19 February 2013

References

Belenkaya, T.Y., Y. Wu, X. Tang, B. Zhou, L. Cheng, Y.V. Sharma, D. Yan, E.M. Selva, and X. Lin. 2008. The retromer complex influences Wnt secretion by recycling wntless from endosomes to the trans-Golgi network. *Dev. Cell*. 14:120–131. http://dx.doi.org/10.1016/j.devcel.2007.12.003

Bonifacino, J.S., and J.H. Hurley. 2008. Retromer. *Curr. Opin. Cell Biol.* 20:427–436. http://dx.doi.org/10.1016/j.ceb.2008.03.009

Boyle, W.J., W.S. Simonet, and D.L. Lacey. 2003. Osteoclast differentiation and activation. *Nature*. 423:337–342. http://dx.doi.org/10.1038/nature01658

Cai, D., M. Zhong, R. Wang, W.J. Netzer, D. Shields, H. Zheng, S.S. Sisodia, D.A. Foster, F.S. Gorelick, H. Xu, and P. Greengard. 2006. Phospholipase D1 corrects impaired betaAPP trafficking and neurite outgrowth in familial Alzheimer's disease-linked presenilin-1 mutant neurons. *Proc. Natl. Acad. Sci. USA*. 103:1936–1940. http://dx.doi.org/10.1073/pnas.0510710103

Chen, D., H. Xiao, K. Zhang, B. Wang, Z. Gao, Y. Jian, X. Qi, J. Sun, L. Miao, and C. Yang. 2010a. Retromer is required for apoptotic cell clearance by phagocytic receptor recycling. *Science*. 327:1261–1264. http://dx.doi.org/10.1126/science.1184840

Chen, H., X. Wu, Z.K. Pan, and S. Huang. 2010b. Integrity of SOS1/EPS8/ABI1 tri-complex determines ovarian cancer metastasis. *Cancer Res.* 70:9979–9990. http://dx.doi.org/10.1158/0008-5472.CAN-10-2394

Crockett, J.C., D.J. Mellis, D.I. Scott, and M.H. Helfrich. 2011. New knowledge on critical osteoclast formation and activation pathways from study of rare genetic diseases of osteoclasts: focus on the RANK/RANKL axis. *Osteoporos. Int.* 22:1–20. http://dx.doi.org/10.1007/s00198-010-1272-8

Cui, S., F. Xiong, Y. Hong, J.U. Jung, X.S. Li, J.Z. Liu, R. Yan, L. Mei, X. Feng, and W.C. Xiong. 2011. APPswe/Aβ regulation of osteoclast activation and RAGE expression in an age-dependent manner. *J. Bone Miner. Res.* 26:1084–1098. http://dx.doi.org/10.1002/jbmr.299

Feinstein, T.N., V.L. Wehbi, J.A. Ardura, D.S. Wheeler, S. Ferrandon, T.J. Gardella, and J.P. Vilardaga. 2011. Retromer terminates the generation of cAMP by internalized PTH receptors. *Nat. Chem. Biol.* 7:278–284. http://dx.doi.org/10.1038/nchembio.545

Guo, J., M. Liu, D. Yang, M.L. Bouxsein, H. Saito, R.J.S. Galvin, S.A. Kuhstoss, C.C. Thomas, E. Schipani, R. Baron, et al. 2010. Suppression of Wnt signaling by Dkk1 attenuates PTH-mediated stromal cell response and new bone formation. *Cell Metab.* 11:161–171. http://dx.doi.org/10.1016/j.cmet.2009.12.007

Hildebrand, D., K. Heeg, and K.F. Kubatzky. 2011. *Pasteurella multocida* toxin-stimulated osteoclast differentiation is B cell dependent. *Infect. Immun.* 79:220–228. http://dx.doi.org/10.1128/IAI.00565-10

Kubota, T., T. Michigami, and K. Ozono. 2009. Wnt signaling in bone metabolism. *J. Bone Miner. Metab.* 27:265–271. http://dx.doi.org/10.1007/s00774-009-0064-8

Lacey, D.L., E. Timms, H.L. Tan, M.J. Kelley, C.R. Dunstan, T. Burgess, R. Elliott, A. Colombero, G. Elliott, S. Scully, et al. 1998. Osteoprotegerin ligand is a cytokine that regulates osteoclast differentiation and activation. *Cell*. 93:165–176. http://dx.doi.org/10.1016/S0092-8674(00)81569-X

Lee, D.H., L.J. Zhou, Z. Zhou, J.X. Xie, J.U. Jung, Y. Liu, C.X. Xi, L. Mei, and W.C. Xiong. 2010. Neogenin inhibits HJV secretion and regulates BMP-induced hepcidin expression and iron homeostasis. *Blood*. 115:3136–3145. http://dx.doi.org/10.1182/blood-2009-11-251199

Liu, Y., Y. Peng, P.G. Dai, Q.S. Du, L. Mei, and W.C. Xiong. 2012. Differential regulation of myosin X movements by its cargos, DCC and neogenin. *J. Cell Sci.* 125:751–762. http://dx.doi.org/10.1242/jcs.094946

Maeda, K., Y. Kobayashi, N. Udagawa, S. Uehara, A. Ishihara, T. Mizoguchi, Y. Kikuchi, I. Takada, S. Kato, S. Kani, et al. 2012. Wnt5a-Ror2 signaling between osteoblast-lineage cells and osteoclast precursors enhances osteoclastogenesis. *Nat. Med.* 18:405–412. http://dx.doi.org/10.1038/nm.2653

McGough, I.J., and P.J. Cullen. 2011. Recent advances in retromer biology. *Traffic*. 12:963–971. http://dx.doi.org/10.1111/j.1600-0854.2011.01201.x

Nakashima, T., M. Hayashi, T. Fukunaga, K. Kurata, M. Oh-Hora, J.Q. Feng, L.F. Bonewald, T. Kodama, A. Wutz, E.F. Wagner, et al. 2011. Evidence for osteocyte regulation of bone homeostasis through RANKL expression. *Nat. Med.* 17:1231–1234. http://dx.doi.org/10.1038/nm.2452

Novack, D.V. 2011. Role of NF-κB in the skeleton. *Cell Res.* 21:169–182. http://dx.doi.org/10.1038/cr.2010.159

Paloneva, J., J. Mandelin, A. Kiialainen, T. Bohling, J. Prudlo, P. Hakola, M. Haltia, Y.T. Konttinen, and L. Peltonen. 2003. DAP12/TREM2 deficiency results in impaired osteoclast differentiation and osteoporotic features. *J. Exp. Med.* 198:669–675. http://dx.doi.org/10.1084/jem.20030027

Pan, C.L., P.D. Baum, M. Gu, E.M. Jorgensen, S.G. Clark, and G. Garriga. 2008. *C. elegans* AP-2 and retromer control Wnt signaling by regulating mig-14/Wntless. *Dev. Cell*. 14:132–139. http://dx.doi.org/10.1016/j.devcel.2007.12.001

Parfitt, A.M., M.K. Drezner, F.H. Glorieux, J.A. Kanis, H. Malluche, P.J. Meunier, S.M. Ott, and R.R. Recker; Report of the ASBMR Histomorphometry Nomenclature Committee. 1987. Bone histomorphometry: standardization of nomenclature, symbols, and units. *J. Bone Miner. Res.* 2:595–610. http://dx.doi.org/10.1002/jbmr.5650020617

Roodman, G.D., and J.J. Windle. 2005. Paget disease of bone. *J. Clin. Invest.* 115:200–208.

Seaman, M.N. 2004. Cargo-selective endosomal sorting for retrieval to the Golgi requires retromer. *J. Cell Biol.* 165:111–122. http://dx.doi.org/10.1083/jcb.200312034

Seaman, M.N. 2005. Recycle your receptors with retromer. *Trends Cell Biol.* 15:68–75. http://dx.doi.org/10.1016/j.tcb.2004.12.004

Seaman, M.N., E.G. Marcusson, J.L. Cereghino, and S.D. Emr. 1997. Endosome to Golgi retrieval of the vacuolar protein sorting receptor, Vps10p, requires the function of the *VPS29*, *VPS30*, and *VPS35* gene products. *J. Cell Biol.* 137:79–92. http://dx.doi.org/10.1083/jcb.137.1.79

Tabuchi, M., I. Yanatori, Y. Kawai, and F. Kishi. 2010. Retromer-mediated direct sorting is required for proper endosomal recycling of the mammalian iron transporter DMT1. *J. Cell Sci.* 123:756–766. http://dx.doi.org/10.1242/jcs.060574

Takeshita, S., N. Namba, J.J. Zhao, Y. Jiang, H.K. Genant, M.J. Silva, M.D. Brodt, C.D. Helgason, J. Kalesnikoff, M.J. Rauh, et al. 2002. SHIP-deficient mice are severely osteoporotic due to increased numbers of hyper-resorptive osteoclasts. *Nat. Med.* 8:943–949. http://dx.doi.org/10.1038/nm752

Tanaka, S., N. Takahashi, N. Udagawa, T. Tamura, T. Akatsu, E.R. Stanley, T. Kurokawa, and T. Suda. 1993. Macrophage colony-stimulating factor is indispensable for both proliferation and differentiation of osteoclast progenitors. *J. Clin. Invest.* 91:257–263. http://dx.doi.org/10.1172/JCI116179

Teitelbaum, S.L. 2000. Bone resorption by osteoclasts. *Science*. 289:1504–1508. http://dx.doi.org/10.1126/science.289.5484.1504

Teitelbaum, S.L., and F.P. Ross. 2003. Genetic regulation of osteoclast development and function. *Nat. Rev. Genet.* 4:638–649. http://dx.doi.org/10.1038/nrg1122

Temkin, P., B. Lauffer, S. Jäger, P. Cimermancic, N.J. Krogan, and M. von Zastrow. 2011. SNX27 mediates retromer tubule entry and endosome-to-plasma membrane trafficking of signalling receptors. *Nat. Cell Biol.* 13:715–721. http://dx.doi.org/10.1038/ncb2252

Vieira, S.I., S. Rebelo, H. Esselmann, J. Wiltfang, J. Lah, R. Lane, S.A. Small, S. Gandy, E.F. da Cruz E Silva, and O.A. da Cruz E Silva. 2010. Retrieval of the Alzheimer's amyloid precursor protein from the endosome to the TGN is S655 phosphorylation state-dependent and retromer-mediated. *Mol. Neurodegener.* 5:40. http://dx.doi.org/10.1186/1750-1326-5-40

Wen, L., F.L. Tang, Y. Hong, S.W. Luo, C.L. Wang, W. He, C. Shen, J.U. Jung, F. Xiong, D.H. Lee, et al. 2011. VPS35 haploinsufficiency increases Alzheimer's disease neuropathology. *J. Cell Biol.* 195:765–779. http://dx.doi.org/10.1083/jcb.201105109

Xiong, F., S. Leonov, A.C. Howard, S. Xiong, B. Zhang, L. Mei, P. McNeil, S. Simon, and W.C. Xiong. 2011a. Receptor for advanced glycation end products (RAGE) prevents endothelial cell membrane resealing and regulates F-actin remodeling in a beta-catenin-dependent manner. *J. Biol. Chem.* 286:35061–35070. http://dx.doi.org/10.1074/jbc.M111.261073

Xiong, J., M. Onal, R.L. Jilka, R.S. Weinstein, S.C. Manolagas, and C.A. O'Brien. 2011b. Matrix-embedded cells control osteoclast formation. *Nat. Med.* 17:1235–1241. http://dx.doi.org/10.1038/nm.2448

Yang, P.T., M.J. Lorenowicz, M. Silhankova, D.Y. Coudreuse, M.C. Betist, and H.C. Korswagen. 2008. Wnt signaling requires retromer-dependent recycling of MIG-14/Wntless in Wnt-producing cells. *Dev. Cell*. 14:140–147. http://dx.doi.org/10.1016/j.devcel.2007.12.004

Yasuda, H., N. Shima, N. Nakagawa, K. Yamaguchi, M. Kinosaki, S. Mochizuki, A. Tomoyasu, K. Yano, M. Goto, A. Murakami, et al. 1998. Osteoclast differentiation factor is a ligand for osteoprotegerin/osteoclastogenesis-inhibitory factor and is identical to TRANCE/RANKL. *Proc. Natl. Acad. Sci. USA*. 95:3597–3602. http://dx.doi.org/10.1073/pnas.95.7.3597

Zhou, Z., D. Immel, C.X. Xi, A. Bierhaus, X. Feng, L. Mei, P. Nawroth, D.M. Stern, and W.C. Xiong. 2006. Regulation of osteoclast function and bone mass by RAGE. *J. Exp. Med.* 203:1067–1080. http://dx.doi.org/10.1084/jem.20051947

Zhou, Z., J.Y. Han, C.X. Xi, J.X. Xie, X. Feng, C.Y. Wang, L. Mei, and W.C. Xiong. 2008. HMGB1 regulates RANKL-induced osteoclastogenesis in a manner dependent on RAGE. *J. Bone Miner. Res.* 23:1084–1096. http://dx.doi.org/10.1359/jbmr.080234

Zhou, Z., J. Xie, D. Lee, Y. Liu, J. Jung, L. Zhou, S. Xiong, L. Mei, and W.C. Xiong. 2010. Neogenin regulation of BMP-induced canonical Smad signaling and endochondral bone formation. *Dev. Cell*. 19:90–102. http://dx.doi.org/10.1016/j.devcel.2010.06.016

Zhu, X.J., C.Z. Wang, P.G. Dai, Y. Xie, N.N. Song, Y. Liu, Q.S. Du, L. Mei, Y.Q. Ding, and W.C. Xiong. 2007. Myosin X regulates netrin receptors and functions in axonal path-finding. *Nat. Cell Biol.* 9:184–192. http://dx.doi.org/10.1038/ncb1535